Marine and Petroleum Geology 108 (2019) 249–271

Contents lists available at ScienceDirect

Marine and Petroleum Geology

journal homepage: www.elsevier.com/locate/marpetgeo

Research paper

Physical property characteristics of gas hydrate-bearing reservoir and associated seal sediments collected during NGHP-02 in the Krishna-Godavari Basin, in the offshore of India

Junbong Jang[a,*], William F. Waite[b], Laura A. Stern[c], Timothy S. Collett[d], Pushpendra Kumar[e]

[a] Integrated Statistics Inc., Contracted to U.S. Geological Survey, Woods Hole, MA, United States
[b] U.S. Geological Survey, Woods Hole, MA, United States
[c] U.S. Geological Survey, Menlo Park, CA, United States
[d] U.S. Geological Survey, Denver, CO, United States
[e] Oil and Natural Gas Corporation, Panvel, Navi Mumbai, India

ARTICLE INFO

Keywords:
India'S national gas hydrate program
Logging-while-drilling
Methane gas hydrate-bearing sediments
Physical properties
Fines characterization

ABSTRACT

India's National Gas Hydrate Program Expedition 02 (NGHP-02) was conducted to better understand geologic controls on gas hydrate occurrence and morphology, targeting coarse-grained sediments along the lower continental slope offshore eastern India. This study combines seismic, logging-while-drilling data, and a petroleum system approach to provide a regional geologic and lithologic context for: 1) gas hydrate morphology and distribution, and 2) effects of fine-grained sediments (clays and other grains smaller than 63 μm) on gas production in NGHP-02 Area B in the Krishna-Godavari Basin. Area B seismic data show a buried anticline/syncline structure with strong reflectors, R1 and R2, that delineate two of the five lithologic units: Unit I (shallowest), II (R1), III, IV (R2) and V (below the bas of gas hydrate stability). Throughout Area B, gas hydrate morphology depends on its placement within these units. Specifically, core- and grain-scale measurements indicate fines content exerts a primary control on the gas hydrate distribution and morphology. Units I, II and III are generally fine-grained. On the anticline crest, these units host primarily grain-displacing gas hydrate veins linked to pore-occupying gas hydrate in thin, localized, coarser-grained deposits. Diatoms in Unit III increase porosity with depth, reaching ~70% where it contacts Unit IV, the gas hydrate reservoir associated with reflector R2. The Unit III lithology and porosity allow fluid and dissolved-phase methane to escape Unit IV and form gas hydrate in the fine-grained overburden. Within Unit IV, fine-grained layers are interbedded with coarser-grained gas hydrate reservoir sands, and the fines content even in the sands is high enough to impact hydraulic and mechanical properties during gas production. Fluid motion during gas production can mobilize fines, which can then clog pore throats, limiting production rates. Pore-water freshening during gas hydrate dissociation can increase fines mobilization, particularly given the smectite identified in the fine-grained interbeds.

1. Introduction

Methane gas hydrate is a crystalline solid in which individual methane molecules are encaged in a lattice of water molecules (Sloan and Koh, 2007), and this methane is considered a potential energy resource. India's National Gas Hydrate Program Expeditions 01 and 02 (NGHP-01 in 2006 and NGHP-02 in 2015, respectively), investigated geologic controls on the occurrence and morphology of gas hydrate in marine sediments offshore eastern India (Fig. 1a). NGHP-01 focused on sites along the upper continental slope and found fracture-filling gas hydrate in fine-grained sediments at most of the tested sites (Collett et al., 2014). NGHP-02 specifically investigated highly gas-hydrate-saturated, sandy sediments closer to the base of the continental slope (Collett et al., 2019; Shukla et al., 2019-b), some of which are potential targets for methane extraction production tests (Boswell et al., 2019; Konno et al., 2019; Myshakin et al., 2019). This study draws from regional and downhole datasets from Area B (Fig. 1b), combined with core-scale physical property measurements and a set of soil classification tests to establish how gas hydrate reservoir and overlying seal sediment characteristics control 1) the gas hydrate distribution and morphology, and 2) the response of the primary Area B gas hydrate reservoir to production via depressurization.

* Corresponding author. U.S. Geological Survey, 384 Woods Hole Road, Woods Hole, MA, 02543, USA.
E-mail address: jjang@usgs.gov (J. Jang).

https://doi.org/10.1016/j.marpetgeo.2018.09.027
Received 10 April 2018; Received in revised form 24 August 2018; Accepted 21 September 2018
Available online 24 September 2018

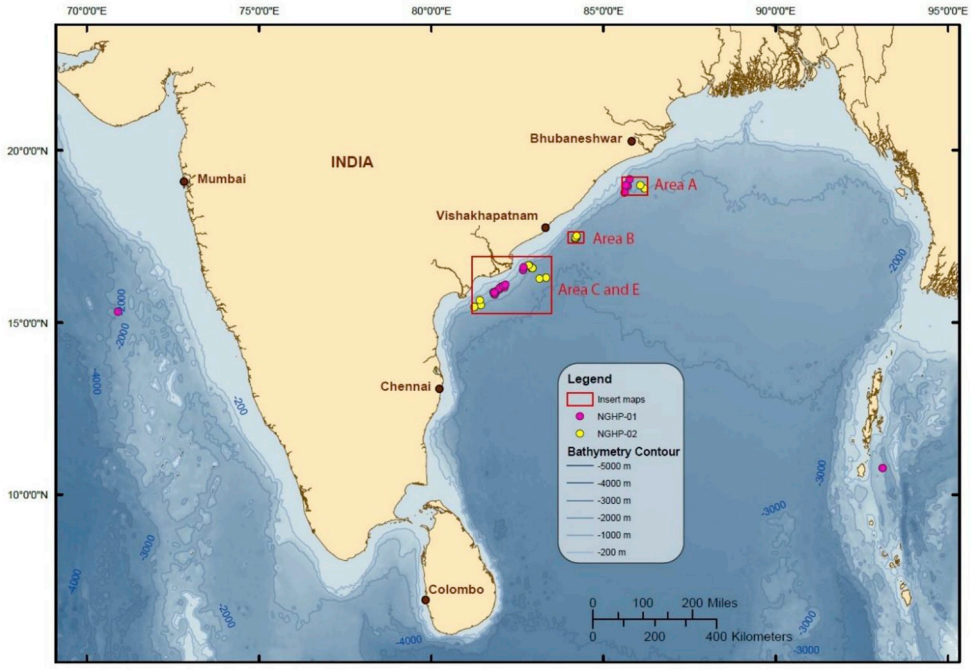

(a)

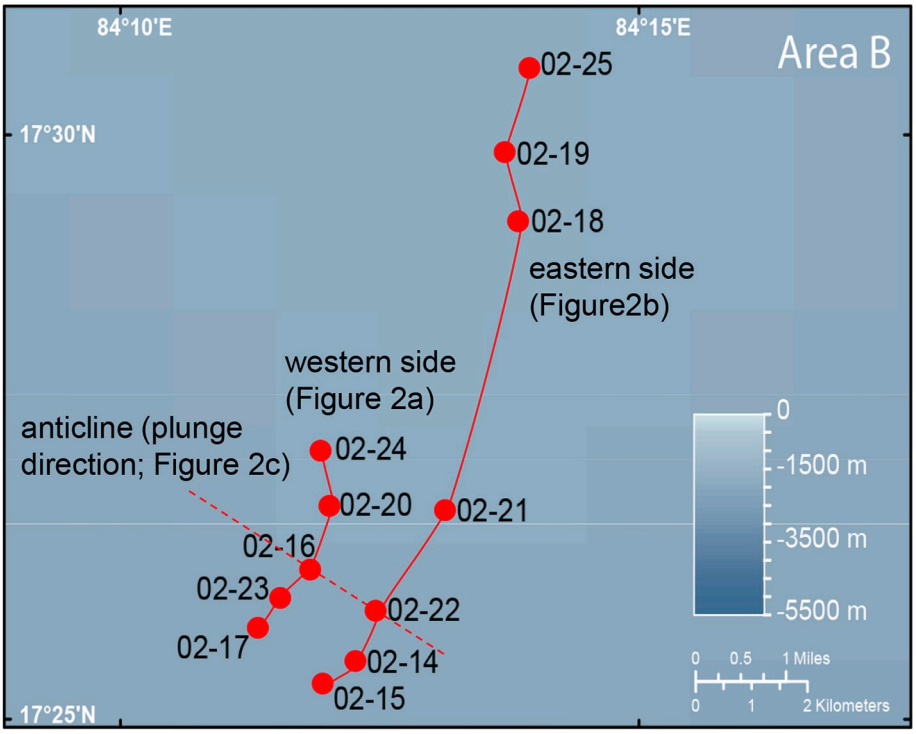

(b)

Fig. 1. (a) The NGHP-02 logging while drilling (LWD) sites used in this study are in Area B, offshore eastern India in the Krishna-Godavari Basin. (b) Of the 12 LWD sites in Area B, coring operations were conducted only at NGHP-02-16, −17, −19, −22 and −23. Subsurface structural linkages between the LWD and coring locations within Area B are imaged in Fig. 2 along the tracklines shown here in red. (For interpretation of the references to color in this figure legend, the reader is referred to the Web version of this article.)

The gas hydrate petroleum system (GHPS) approach has four components that provide a useful structure for understanding sediment property control on gas hydrate occurrences: 1) pressure and temperature conditions within the gas hydrate stability field, 2) suitable methane and water supply, 3) reservoir sediment suitable for storing gas hydrate, and 4) an effective seal for preventing methane escape

from the reservoir (Collett et al., 2009; Max and Johnson, 2014). Following the approach of Waite et al. (2019-b), components 1 and 3 are linked here as an "effective reservoir quality," reflecting the combined requirements for gas hydrate stability and storage space. Components 2 and 4 are linked as an "effective methane availability", reflecting a competition between methane supplied to the reservoir, and methane lost from the reservoir due to an imperfect seal. As a general approach, seismic and logging-while-drilling (LWD) data are used here to provide a basis for delineating and characterizing GHPS reservoir and seal elements. Within these lithologic elements, the sediment analysis and soil classification studies provide insight into the NGHP-02 research questions regarding connections between the geologic environment and the gas hydrate morphology, distribution, and system response to methane extraction via depressurization.

Effective reservoir quality: All NGHP-02 sites cored in Area B are in water deeper than 2500 m, with bottom-water temperatures below 2.5 °C (Collett et al., 2019; Waite et al., 2019-b), so the gas hydrate stability zone extends at least 270mbsf (meters below seafloor) for these sites (Waite et al., 2019-b). A sediment-scale analysis, particularly regarding the fines, provides a basis for assessing not only the morphology of gas hydrate present in the sediment (Dai et al., 2012; Jain and Juanes, 2009), but also the distribution of gas hydrate. In NGHP-02, a correlation between clay content (grains less than 4 μm across) and gas hydrate saturation indicates gas hydrate will not form if the clay content is 30% or higher (Waite et al., 2019-b; Oshima et al., 2019).

The sediment-scale analysis of the effective reservoir quality also provides insight into the reservoir response to depressurization. Based on data compiled by Park and Santamarina (2017), for example, the fines content in a coarse-grained sediment can be enough for sediment permeability, compressibility and strength to become dominated by the properties of the fine sediment rather than the coarse sediment.

In addition to the fines content, the type of fines present is also important to establish, particularly for production applications in which gas hydrate is destabilized. As reported in Jang et al. (2018a), fines exposed to the pore-water freshening that occurs during gas hydrate dissociation can, depending on the type of fines, become more or less prone to getting resuspended in the pore fluid, swept toward the production well, clogging pore throats and reducing production efficiency.

Effective methane availability: A complimentary perspective on gas hydrate distribution and reservoir response can be obtained from the sediment analysis and soil classification study of reservoir, interbed and seal sediments. Collett and Kvenvolden (1988) and Max and Johnson (2014) view the gas hydrate reservoir itself as a "seal" unit due to the extreme permeability reduction that occurs in coarse-grained material hosting high gas hydrate saturations. For Sites NGHP-02 08 and 09 in Area C, however, the LWD-based continuous downhole log of permeability indicates the fine-grained sediment that overlies the primary gas hydrate reservoir is one to three orders of magnitude less permeable than the highly gas hydrate-saturated reservoir sediment (Waite et al. 2019-b).

The presence of a low-permeability layer overlying coarser-grained, reservoir-quality sediment is important for improving the production efficiency of the reservoir (Ajayi et al., 2018; Konno et al., 2019), but may also be important for forming gas hydrate in the reservoir in the first place, particularly where the methane supply is determined by microbial production rates. Methane supply is a critical third requirement for gas hydrate formation in addition to the pressure and temperature requirements. In marine settings, methane hydrate is generally inferred to form from methane dissolved in pore water (Collett et al., 2009), but formation cannot occur until the pore-water methane concentration exceeds the local methane solubility concentration.

For NGHP-02, the methane source is primarily microbial (Collet et al., 2019; Dixit et al., 2019; Holland et al., 2019), so pore water methane concentrations depends on the balance between microbial production rates and pore-water flow rates. Using a simplistic, 1-dimensional flow environment as a conceptual example, if sediment overlying a coarse-grained reservoir has very low permeability, the vertical migration of pore fluid can be slowed. Slower flow provides time for microbial production to yield higher pore-water methane concentrations. As shown by Xu and Ruppel (1999), the methane solubility falls for pore water migrating upward into cooler sediment, meaning pore water with higher initial methane content is able to begin precipitating gas hydrate at deeper depths. If the sediment overlying a potential coarse-grained gas hydrate reservoir has low permeability, that can potentially help to slow the upward migration of pore water enough to enable microbial activity to generate methane concentrations high enough to initiate gas hydrate growth even near the base of gas hydrate stability.

Unlike Area C, no LWD permeability measurement was made for the Area B sediment overlying the primary gas hydrate reservoir. To estimate the permeability of the Area B overburden sediment and address the effective methane availability issue, this study includes a set of sediment property measurements. One conclusion presented this work is that, like Area C, the overlying sediment at Area B is of lower permeability than the gas hydrate-bearing reservoir sediment. In this work, the overlying fine-grained sediment in Area B is therefore considered to be the "seal," which is the arrangement originally adopted for the conventional petroleum system (Magoon, 1988; Perry, 1988).

2. Methods

The tools and techniques used to obtain physical property results for this study are summarized in this section. The geologic framework and lithology (Sections 3 and 4, respectively) are based on compiled data from pre-cruise seismic surveys (Collett et al., 2019; Shukla et al., 2019-b) and NGHP-02 LWD results discussed here. Within that geologic framework, the science questions regarding gas hydrate morphology, distribution and sediment response to gas production activities are addressed with a combination of LWD and discrete sediment test results.

2.1. Downhole LWD measurements

LWD data provide a framework of continuous downhole physical property profiles, and a complete discussion of the LWD tools utilized during NGHP-02 is provided by Kumar et al. (2019). This study draws on indicators of gas hydrate occurrences from logs of the bulk density (ρ_b), natural gamma ray (NGR), mineral component content (Quartz/Feldspar/Mica, denoted QFM) and clay content, compressional wave velocity (V_p), and electrical resistivity logs. A table of tool descriptions and gas hydrate indicators for these devices is presented by Waite et al. (2019b).

2.1.1. Porosity

Porosity is measured in two ways, using LWD to infer a continuous downhole porosity profile, and using sediment core testing to provide direct, discrete measurements. LWD estimates of porosity are derived from the LWD bulk density measurements. Bulk density, ρ_b, is taken from the Schlumberger EcoScope tool, which analyzes returns from gamma rays emitted by the tool into the formation. Bulk densities are used here to calculate the "density porosity," ϕ_D, following the approach of Lee and Collett (2011):

$$\phi_D = \frac{\rho_g - \rho_b}{\rho_g - \rho_f}, \quad (1)$$

where ρ_f is the density of the pore filling material, assumed here to be that of seawater, 1.03 g/cm^3 for consistency with other NGHP-01 and -02 investigations (Collett et al., 2008; Waite et al., 2019-a; b). In Equation (1), ρ_g is the grain density obtained from the core-based laboratory test described in Section 2.2.

Discrete, core-based porosity measurements are calculated from shipboard moisture and density measurements made on small sediment samples. The dry water content, which is the ratio of water mass to solid mass without salt, provides the water volume, and the solid volume is measured using a Quantachrome pycnometer. Porosity is calculated as the volume of water divided by the combined volume of the water and solids.

2.1.2. Natural gamma ray (NGR)

Gamma radiation is naturally emitted by only a few elements, and those emissions can be detected by the Schlumberger EcoScope Tool (Adolph et al., 2005). High gamma ray emissions are generally associated with clays, but when interpreting NGR results for Area B, the reverse is true. Coarse-grained intervals in NGHP-02 Area B have elevated levels of mica, which is a gamma-ray emitter due to its potassium content (Sundal et al., 2016). Consequently the coarse-grained gas hydrate reservoir layers tend to have higher natural gamma responses than that of the adjacent fines.

2.1.3. Mineral component content (QFM-clay)

The Schlumberger Spectrolith tool emits neutrons into the formation and detects gamma rays returning from interactions between the neutrons and certain chemical elements in the sediments (Schlumberger, 2006). Based on the measured gamma-ray energies, estimates of the chemical composition and concentrations of various mineral components are inferred. This study utilizes the tool-inferred mineral contents for the combined QFM (as a proxy for coarse-grained sediment content), clay, calcite and pyrite.

2.1.4. Compressional wave velocity (V_p)

Of the sites that were cored and discussed here in Area B, the Schlumberger sonicVISION tool was used for Sites NGHP-02-16 and −17, and the Schlumberger SonicScope tool for Sites NGHP-02-19, −22 and −23. Each tool provides V_p in the formation. Elevated V_p is inferred to indicate the presence of gas hydrate, which increases sediment stiffness (Yun et al., 2005; Lee and Collett, 2011; Shankar, 2016; Joshi, 2019).

2.1.5. Electrical resistivity

The Schlumberger GeoVISION tool (Bonner et al., 1996) measures the electrical resistivity of the formation, indicating the presence of gas hydrate based on gas-hydrate's electrically insulative qualities relative to the conductive pore water. The GeoVISION tool yields resistivity-based borehole images, the brightness and shapes of which indicate the presence of gas hydrate. The borehole images can also be used to distinguish between the two gas hydrate morphologies observed in Area B. In the shallower fine-grained sediment, gas hydrate-filled fractures are the dominant morphology, and these dipping fractures can be observed as bright, sinusoidal traces in the resistivity image. At greater depths, and where coarser grains are present, gas hydrate primarily grows in existing pore space and can form an interconnected network capable of supporting a portion of the overburden load. Defined here as “pore-filling” (or “pore-occupying”), this morphology appears as bright, thick, flat regions in the resistivity image. Resistivity data were also used by Collett et al. (2019) to infer the downhole distribution of fracture-filling and pore-filling gas hydrate at each site. The resistivity-based gas hydrate saturations tend to be over-predicted where fracture-filling gas hydrate is present (Lee and Collett, 2009; Cook et al., 2010), but the results are still effective in delineating the depth interval where gas hydrate-filled fractures exist.

2.2. Laboratory tests on recovered sediments

Shipboard and post-cruise measurements include systemic testing of recovered core material to provide downhole index property data for ground truthing LWD interpretations. Additionally, given the significance of the primary gas hydrate accumulation near the anticline crest in Area B as a potential production target (e.g. Lin et al., 2019; Myshakin et al., 2019; Uchida et al., 2019; Konno et al., 2019), samples from the overburden, reservoir and underlying sediment along the anticline crest were collected for additional geotechnical testing.

2.2.1. Downhole profile properties

2.2.1.1. Grain size distribution. Shipboard grain size measurements on the *D/V Chikyu* and post-cruise measurements at the U.S. Geological Survey (USGS) were conducted using a multi-wavelength laser particle size analyzer (PSA), Beckman Coulter, model LS13320, which measures grain sizes from 0.375 μm to 2 mm. Specimen preparation and measurements follow standard IODP procedures (e.g. Expedition 331 Scientists, 2011). Additional steps were taken for the USGS specimens, where sieves were used to establish the grain size distribution for grains above 2 mm in diameter, with smaller particles being measured with the PSA. See Waite et al. (2018 c) for USGS data and procedures. Grain sizes are given in d_x notation, e.g., d_{10} is the grain size for which 10% of the specimen (by mass) is smaller than the d_{10} value. For both the shipboard and post-cruise grain-size distributions, muds are defined as the grains that are silt-sized and smaller (Folk, 1954), and have a maximum grain diameter of 63 μm. Clays are grains with less than 4 μm-diameters.

2.2.1.2. Grain density (ρ_g). Grain densities were calculated from the measured dry sediment mass and volume. The volume measurements for both the *D/V Chikyu* and USGS core samples were conducted using a helium-displacement five-cell pycnometer (Pentapycnometer 5200e, Quantachrome Instruments). Grain densities were incorporated into Equation (1) to estimate the LWD density-porosity.

2.2.2. Lab tests for selected five samples

To better understand how the primary Area B gas hydrate reservoir system near the crest of the anticline would respond to the changes in effective stress and pore-water freshening imposed during production activities, five samples were collected for additional geotechnical testing. Samples were recovered from the reservoir overburden, the reservoir itself, and the underlying sediment (Table 2). Only small amounts of sediments were available, limiting the experimental methods to the following:

2.2.2.1. Microscopic images. A Leica DMS1000 stereomicroscope was used to acquire images of the overall particle shape and clustering in air at low magnification. A Tescan VEGA-3 variable-pressure scanning electron microscope (SEM) equipped with energy dispersive spectroscopy (EDS) provided more detail on features of the coarse and fine particles. Samples were first imaged by cryogenic SEM methods using the SEM's specialized cryo-preparation and imaging stage (Gatan Alto 1000 model) in order to assess the textural arrangement of grains within the originally damp samples, which were quenched in place by liquid nitrogen in the cryo-preparation station. Cryo-SEM imaging was conducted below 180 °C, with accelerating voltage of 10–15 kV, and in low-vacuum mode at a pressure of 20–30Pa. All samples were then room- or oven dried, and re-imaged at room temperature SEM conditions using high-vacuum, low-voltage techniques for improved image resolution of very fine grained sediments and/or sub-micron detail in microfossils. The reservoir-sandy interbed and the overburden seal specimens were screened by a 75 μm sieve to separate coarse and fine grains to compare SEM images for each size fraction.

2.2.2.2. X-ray diffraction, XRD. A Rigaku Miniflex 600 benchtop X-ray diffraction unit was used to identify mineral phases and their relative abundances through X-ray powder diffraction analysis. The device uses a copper anode tube for X-ray generation, and is operated at 40 kV, 15 mA. Dry powdered samples were prepared on slides, loaded into the

Table 1
Gas hydrate zones in Area B, NGHP-02 (mbsf – meter below seafloor; the site number is listed as NGHP-02-xx).

No. site	water depth [m]	seismic reflectors [mbsf]		BSR [mbsf][b]	gas hydrate occurrence [mbsf]		lithological units[b]				
		R1	R2		top	bottom	I	II	III	IV	V
14	2565.0	213.5–238.4	N/A	285	65.3	251.8					
15	2569.0	221–241	N/A	290	60.2	285.6					
16	2546.5	176.5–181.5	272.5–296.8	290	64.2	291[a]	0–177.7	177.7–187.4	187.4–273.2	273.2–296.2	296.2-
17[a]	2558.0	171.3–175.8	259.3–290.3	288.2	58.9	287[a]	0–173.0	173–175.3	175.3–271.8	271.8–313.1	313.1-
18	2520.5	301.2–353.6	N/A	325	102.3	353.6					
19[a]	2519.5	305.2–372	N/A	330.9	100.0	325[a]	0–305.3	305.3–370.7	370.7-	N/A	N/A
20	2540.5	160.1–167.9	272.6–291.3	300	91.7	290.0					
21	2543.0	N/A	N/A	295	68.2	310.9					
22[a]	2556.0	207.7–234.8	368.6–386.5	280	70.6	290[a]	0–211.2	211.2–228.4	228.4–364.4	364.4–370.0	370.0-
23[a]	2553.0	181.3–188	300.8	290	47.0	292[a]	0–181.1	181.1–187.5	187.5–271.2	271.2–299.6	299.6-
24	2531.0	188.4–191	309.5–344.9	309.6	288.2	305.0					
25	2518.5	301.9–375.6	N/A	320	128.6	375.6					

[a] Gas hydrate occurrences defined by core measurements and LWD data (Waite et al., 2019a).
[b] Defined by Collett et al. (2019). All others are compiled from shipboard-acquired data.

internal goniometer, and analyzed for 2θ = 3°–90° with a step size of 0.02° and scan rate of 0.5°/minute. Additional sample preparation methods are described by Poppe et al. (2001). Data processing and analysis was completed using the Rigaku PDXL2 software. Whole powder pattern fitting was used for quantitative phase analysis and the Rietveld method was used for structure refinement.

2.2.2.3. Specific surface (S_s). The wet method was used to determine specific surface [m^2/g] using methylene blue (Santamarina et al., 2002). The dry sample was mixed with water to separate particles, and the methylene blue solution was added using a pipette with a metered droplet delivery until the methylene blue ions covered all particle surfaces. The specific surface, S_s was calculated from:

$$S_s = \frac{c_{MB} V_{inc} N_{drop} N_{Avo} A_{MB}}{M_{soil}}, \quad (2)$$

where c_{MB} [mol/L] is the concentration of methylene blue, V_{inc} [L] the volume of methylene blue solution per drop, N_{drop} the number of methylene blue solution drops added to the sample mixture, N_{Avo} [1/mol] the Avogadro's number, A_{MB} [m^2] the surface area each methylene blue ion covers, and M_{soil} [g] the mass of soil.

2.2.2.4. Liquid and plastic limits. For the Atterberg limits, which are indices describing the sediment consistency, the liquid limit (*LL*) and plastic limit (*PL*) were measured. The liquid limit test used the cone penetrometer method (BSI, 1990), and the plastic limit test followed ASTM D4318 (ASTM, 2005). The plasticity index PI is defined as the difference between the liquid limit and plastic limit: *PI=LL-PL*. Of the five sediment specimens collected for this portion of the study, only the specimen from the underlying sediment was large enough to conduct *LL* and *PL* tests.

Electrical Sensitivity, S_E. The electrical sensitivity, determined from the liquid limits measured separately with deionized water, 2M-brine and kerosene (Jang and Santamarina, 2016, 2017), provides insight into the sediment properties and response to pore-fluid chemistry changes such as the pore-water freshening that occurs during gas hydrate dissociation (Hesse and Harrison, 1981). In this study, due to the lack of recovered sediment volume for each sample, the electrical sensitivity test was only conducted on the underlying sediment, and the required liquid-limit measurements in the different fluids could only be accomplished by recycling the sample material. For the first liquid limit measurement, the sample was tested using deionized water. The sample was then dried in preparation for the liquid limit test with 2M-brine,

Table 2
Physical properties of the five specimens selected for additional geotechnical testing.

Site No.		NGHP-02-16			NGHP-02-23	
sample ID		633170	640170	634470	585170	590470
sample information		NGHP-02-16B-4P-5, 10.0–22.0 cm	NGHP-02-16B-4P-4, 0.0–11.0 cm	NGHP-02-16B-7P-2, 110.0–120.0 cm	NGHP-02-23B-29X-9, 74.0–86.0 cm	NGHP-02-23B-33X-2, 64.0–74.0 cm
depth [mbsf]		278.2	278	285.6	262.9	295.2
lithology		sand	sand	pelagic-poor clay	clayey-silt	clay
sediment type		reservoir-fine sand	reservoir-sandy interbed	reservoir-clay interbed	overburden seal	underlying seal
bulk density [kg/m^3]		1470.9	1993.1	2103.2	1501.1	1851.4
grain density [kg/m^3]		2713	2717	2749	2448	2744
porosity [ ]		0.3848	0.354	0.442	0.6924	0.5322
particle size	d_{10} [mm]	0.017	0.004	0.0026	0.0021	0.0011
	d_{30} [mm]	0.041	0.019	0.011	0.0053	0.0028
	d_{50} [mm]	0.0903	0.0356	0.0219	0.0103	0.0053
	d_{60} [mm]	0.101	0.048	0.028	0.013	0.007
	d_{90} [mm]	0.3067	0.1722	0.0677	0.0478	0.0194
	sand [%]	60.7	32.3	11.3	5.2	0.3
	mud [%]	39.3	67.7	88.7	94.8	99.7
specific surface [m^2/g]		5.8	11.5	35.6	92	69
LL_{DW} before dilution						74
LL after dilution	LL_{DW}					61
	LL_{brine}					53
	LL_{ker}					46
S_E						0.31
PL						30

then re-saturated with 2M-brine. After the liquid limit test with 2M-brine, the sample was diluted in 1000 ml cylinders, allowed to settle, and when the supernatant became transparent, the supernatant was siphoned off. This process was repeated until the pore-fluid achieved low salinity. After drying the washed sediment, the sample was saturated with kerosene and the liquid limit test with kerosene was conducted. Because this recycling process can involve a curing effect between fines, it is recommended that electrical sensitivity testing use fresh remolded-sediment whenever possible.

2.2.2.5. Sedimentation test. The grain-settling-rate-based sedimentation tests provide insight into how the morphology and mineralogy of particles affect sediment fabric formation as a function of different pore fluid chemistry (Pierre and Ma, 1999; Palomino and Santamarina, 2005; Jang et al., 2018a). Since the fabric formation determines the sediment compressibility and permeability, sedimentation test results show how sediment compressibility and permeability will likely evolve as the in situ system transitions from saline to freshened pore water during gas hydrate dissociation triggered as methane is extracted from the reservoir.

Following the approach of Jang et al. (2018a), dry sediment was loosely packed in a cylindrical mold to a height and diameter of 25.4 mm to obtain a minimum bulk density sample for each test. The prepared sediment was then mixed with the test fluid and allowed to equilibrate for at least 12 h in an 80 mL beaker. The mixture was then poured into a cylinder of 25.4 mm diameter and 190 mm height, setting the column height of the mixture to 152.4 mm. The cylinder was vacuumed for 30 min to remove air from the mixture. After the vacuum process, the sediment fluid mixture was shaken for one minute and allowed to settle until the settled sediment height became constant (1–4 days).

When the original marine sediment was dried, salt from the in situ pore-fluid precipitated as a solid material. Thus, the initial laboratory mixture of dry sediment with deionized water contained dissolved salt, and was identified as a “deionized water with salt” sample (DWS). In order to reduce the effect of salt, approximately 80% of the supernatant fluid in the cylinder was removed after the initial sedimentation test. The cylinder was refilled with deionized water, so the mixture contained freshened water and was identified as a “deionized water, freshened” sample (DWF). The sedimentation test was repeated with the freshened water mixture. Separately, subsamples of the original marine sediment were dried and tested with their in situ salts, using a 2M-brine solution and kerosene like the electrical sensitivity tests. Sediment mixtures with 2M-brine and kerosene were not recycled in the sedimentation tests.

3. Geological structure of area B

Fig. 1 shows the locations of the drilling sites in each area during NGHP-02. A detailed discussion of the Area B geologic structure, as well as the relationships between the prominent seismic reflections, lithologic units and primary gas hydrate occurrences is provided by Collett et al. (2019) and Shukla et al. 2019-a, b. A summary is given here to provide a geological context for this study's physical property and sediment analysis results.

Krishna-Godavari Basin is a passive margin, and the northeast - southwest trending horst-graben rift system is covered by recent Quaternary alluvium sediment layers (Rao, 2001; Radhakrishna et al., 2012). Beneath the younger sediments, seismic reflection data for Area B in the Krishna-Godavari Basin reveals a buried anticline that plunges in the northwest - southeast direction due to local compressive stresses. Fig. 1b shows a map view of the LWD and coring sites in Area B, as well as three seismic sections tracking along the anticline near its crest (Fig. 2a), along its eastern flank (Fig. 2b), and tracking across the anticline in the plunging direction (Fig. 2c). The prominent reflectors R1 and R2 in Fig. 2 are associated with specific lithologic units (described in Section 4). These reflectors and the bottom-simulating reflector (BSR), associated with the base of hydrate stability (Shukla et al., 2019-b), serve to delineate the anticline structure and indicate the lithologic unit depths relative to the gas hydrate stability field. Given the strong bias toward microbial methane as the primary guest molecule in the NGHP-02 Area B gas hydrate (Collett et al., 2019; Dixit et al., 2019; Holland et al., 2019), the BSR is assumed here to indicated the stability boundary for structure I gas hydrate.

Near the anticline crest, (Fig. 2a, c), R1 is not prominent, but R2 is strong and closely associated with the BSR (Shukla et al., 2019-b). Along the anticline crest, R2 represents the primary gas hydrate reservoir target, and indicates the gas hydrate accumulation is just above the base of gas hydrate stability (Collett et al., 2019; Shukla et al., 2019-b; Waite et al., 2019-a). The stratigraphic relationships from the anticline crest (represented by Site NGHP-02-16) to the southeast along the flank of the anticline (represented by Site NGHP-02-22) are best seen in the seismic line depicted in Fig. 2c, which shows R1 and R2 follow the plunging contour of the anticline. Just off the anticline crest, R2 plunges through the BSR and below the base of gas hydrate stability. Even R1 passes through the BSR and is buried below the base of gas hydrate stability further down the anticline flank. This type of anticlinal structure, pushing up into the gas hydrate stability zone, has been proposed by Kvenvolden (1993) as an effective gas hydrate reservoir geometry and been observed elsewhere such as in the Ulleung Basin (Ryu et al., 2013) and Gulf of Mexico (Boswell et al., 2012). To the northeast, the anticline transitions to a syncline where R1 appears to merge with the BSR (right side of Fig. 2b).

To test the relationships between these reflectors and the Area B lithology, NGHP-02 acquired data from LWD drilling Sites NGHP-02-16, −17, −20, −23 and −24 on the crest of the anticline (Fig. 2a), Sites NGHP-02-14, −15, −21 and −22 on the slope of the anticline (Fig. 2b), Site NGHP-02-18 on the lower flank of the anticline, and into a syncline at sites NGHP-02-19 and −25 to the northeast of the Area B anticline (Fig. 2b). In addition to LWD drilling, coring was conducted at five Area B sites: NGHP-02-17, −19, −22 and −23 were tested with pressure coring (Holland et al., 2019) and conventional coring (Kumar et al., 2019); Site NGHP-02-16 was only pressure cored. Approximate sub-bottom depths for the R1, R2 and BSR reflectors at each of these sites are given in Table 1.

4. Lithologic controls on gas hydrate occurrences in area B

During the NGHP-02 expedition, five lithologic units have been defined for Area B based on recovered cores (Fig. 3). Table 1 lists the depths for the reflectors, lithologic units and gas hydrate occurrences for the five drill sites in Area B. The lithologic units are defined as:

- Unit I is a variegated unit containing gas hydrate-filled fractures (particularly in the lower portion), hemipelagic silty clay, and mass transport deposits (MTDs) composed of mud clasts in muddy matrices. The MDT matrices consist of light-colored clay, a volcanic ash fall, and thinly bedded sand that is rich in quartz, calcareous bioclasts and lithic fragments. Micro- and nannofossils are also present in this unit. As described by Collett et al. (2019), the gas hydrate-filled fractures (grain-displacing gas hydrate) appear to be linked to (and possibly sourced by) pore-filling gas hydrate in the thin, localized, coarse-grained deposits within Unit I.
- Unit II generally correlates with the R1 reflector (Table 1). Unit II is thin near the anticline crest, thickening downslope toward NGHP-02-19. Unit II exhibits high natural gamma ray log values and contains authigenic carbonate-bearing silty clay and mica (mostly biotite)-bearing sand. The unit lacks pelagic grains and both calcareous and siliceous microfossils. Gas hydrate distributions inferred from LWD electrical resistivity measurements (Collett et al., 2019) show Unit II has only sporadic occurrences of gas hydrate, generally in isolated intervals rather than throughout the unit. The gamma,

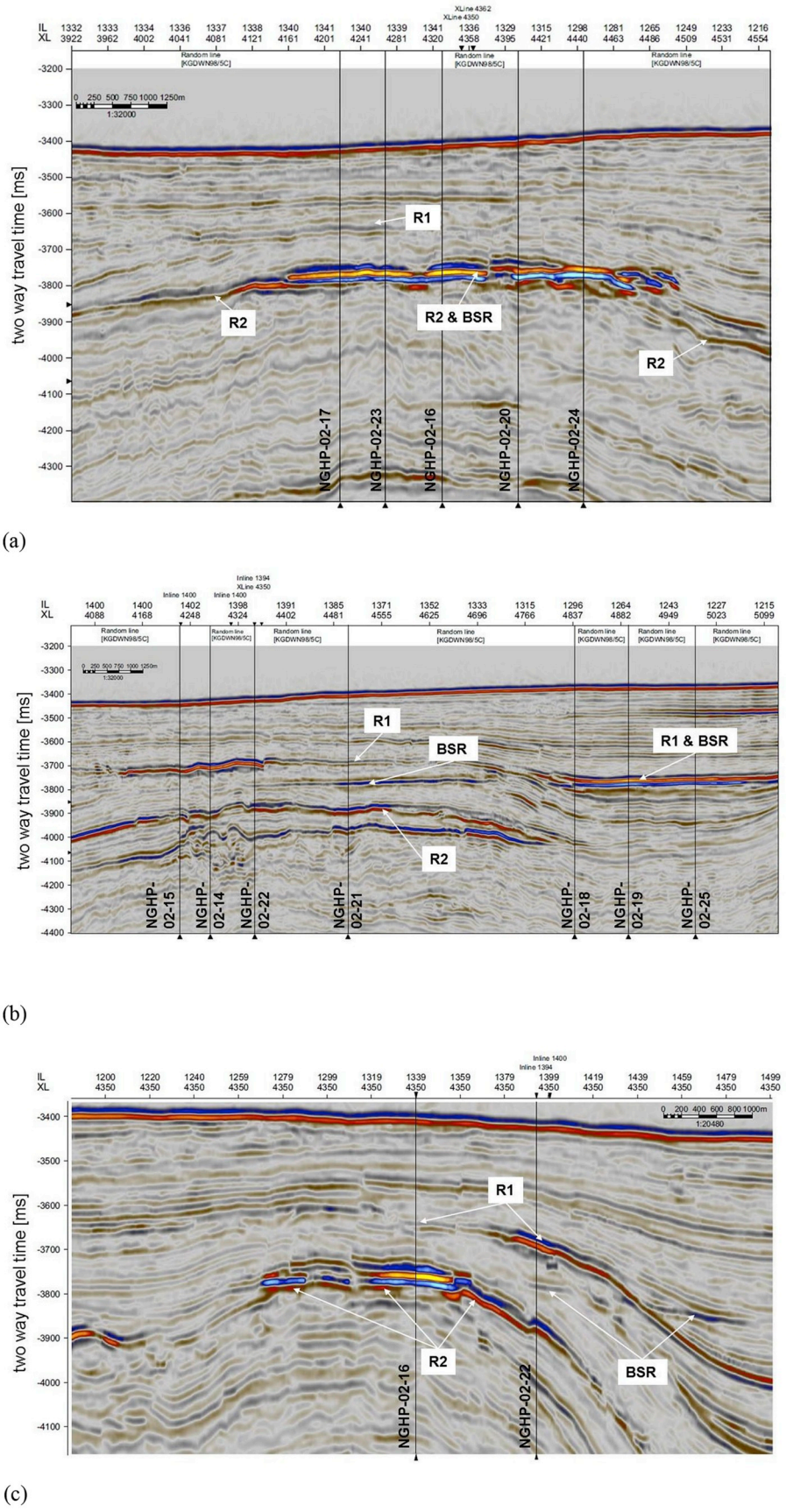

Fig. 2. Seismic reflection profile slices for a 3D seismic dataset for Area B, showing the spatial relationships between the two primary seismic reflections in the region (R1 and R2), and the bottom-simulating reflector (BSR) (a) Sites on the anticline crest, the western transect from Fig. 1. These sites penetrate the primary gas hydrate reservoir in Area B, which is associated with R2. This reservoir sits just above the base of hydrate stability (Collett et al., 2019; Waite et al., 2019a), as indicated by the BSR reflection just below R2 (Shukla et al., 2019b) (see also Fig. 2c); (b) Seismic profile slice along the eastern transect from Fig. 1. Transect runs along the eastern flank of the anticline through sites NGHP-02-14, −15, −21, −22 on the left portion of the figure, extending off down the anticline flank through NGHP-02-18 and into the syncline (NGHP-02-19, −25) on the right portion of the figure. In the syncline, the primary gas hydrate reservoir is again just above the base of hydrate stability as suggested by R1 lying just above, and nearly collocated with, the BSR; (c) cross line passing through the anticline crest at NGHP-02-16, and down the anticline flank through NGHP-02-22. The BSR is faintly observable, separating from R2 and cutting across the R1 reflector as the R1 and R2 sediments (Units II and IV, respectively, Fig. 3) follow the anticline contour and plunge below the base of gas hydrate stability. Additional representations of the Area B subsurface structure in relation to the reflectors and NGHP-02 drill sites are provided by Shukla et al. (2019-a, b).

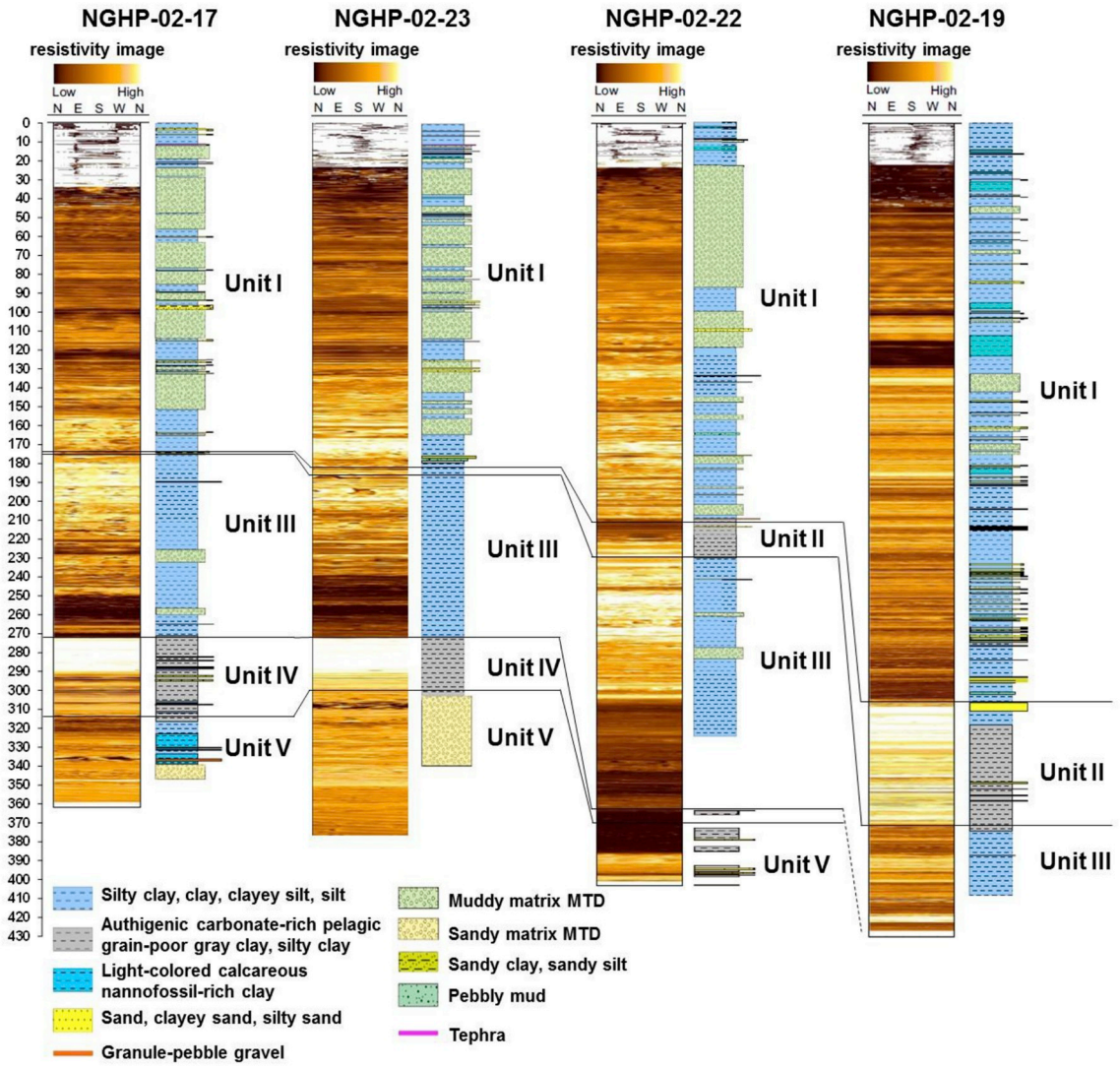

Fig. 3. Area B lithology profile schematic. For the four sites with essentially continuous coring, summaries are presented here for the electrical resistivity-at-the-bit (left image for each site), lithology taken from the shipboard visual core descriptions (right image), and the labeled lithologic Units I-V. The lithology legend is given below the downhole data. Gas hydrate is found in the lower portion of the fine-grained, MTD-bearing Unit I, and to a limited extent in Unit II. Gas hydrate is more prevalent in the fine-grained, diatom and microfossil-rich Unit III. Unit IV is an interbedded unit with thinly-bedded fine sands alternating with clay-rich intervals. On the anticline crest (NGHP-02-17 and 23), the top of Unit IV is associated with the primary gas hydrate accumulation and is indicated by the white band of high resistivity. Unit IV shifts below the BSR on the anticline slope (NGHP-02-22), and the primary hydrate accumulation transitions to the upper portion of Unit III. Unit V marks a return to fine-grained sediment beneath the primary gas hydrate reservoir sediments.

QFM and grain size values for Unit II are higher than in the adjacent Units I and III. By analogy to Unit IV, which also has elevated gamma QFM and grain size responses that are attributed to relatively low clay-content and fine, mica-bearing sands, it is possible that Unit II has low clay content, coarser grained sediment relative to the adjacent Units I and III. This interpretation has led to the inference that Unit II is permeable enough to act as a conduit for methane migrating up toward the anticline crest (Saito et al., 2019), but this interpretation is not definitive (Collett et al., 2019).

- Unit III contains gas hydrate-filled fractures, which like those in Unit I, appear to link with pore-filling gas hydrate in thin, localized, coarse-grained deposits (Collett et al., 2019). The lithology of the unit is diatom-rich, calcareous-nannofossil-bearing silty clay that is associated locally with medium-sand-sized black lithic fragments scattered in the lower part of the unit. The gas hydrate-filled fractures are generally associated with the anticline crest, and they are thought to be fed by methane that migrated up to the anticline crest via the relatively permeable Units II and IV (Saito et al., 2019).
- Unit IV generally correlates with the R2 reflector (Table 1). Near the anticline crest, Unit IV is a highly gas hydrate-saturated reservoir interval. The Unit IV sediment is characterized by high natural gamma ray log values and contains authigenic carbonate-rich silty clay and mica-(mostly biotite)-bearing sand laminae with wood fragments (Hsiung et al., 2019; Nanda et al., 2019). Unit IV lacks pelagic grains and both the calcareous and siliceous microfossils that are abundant in Unit III. Along the anticline crest, just above the BSR, Unit IV hosts the primary gas hydrate-bearing reservoir section for Area B in a series of thinly-bedded coarse-grained layers (fine sands) with pore-filling gas hydrate. These layers are intercalated with fine-grained sediment with little-to-no gas hydrate. Unit IV is expected to be a relatively permeable, dipping layer on the anticline flank and is inferred by Saito et al., (2019) to supply methane to the anticline crest.
- Unit V is the underlying sediment beneath the primary gas hydrate reservoir on the anticline crest, and plunges below the deepest penetration at NGHP-02-19and −22. Unit V is characterized by

calcareous nannofossil-rich silty clay MTDs composed of silt, silty clay clasts, coral fragment and microfossils in a sandy matrix.

Variations in sediment physical properties between units, combined with site-to-site variations in the burial depth and thickness of each unit, result in site-specific effective reservoir quality and effective methane availability. To characterize these modified gas hydrate petroleum system elements, continuous LWD profiles and discrete core sediment measurement results are presented here for the five sites drilled in Area B during NGHP-02. These results are combined in Section 6 with additional soil testing results (Section 5) to discuss local geologic controls on gas hydrate morphology, distribution and the system's response to methane extraction via depressurization.

4.1. Anticline crest: sites NGHP-02-16, NGHP-02-17 and NGHP-02-23

Sites NGHP-02-16, −17 and −23 penetrate the crest of the anticline in Area B and because they show similar downhole physical property profiles, they are dealt with together here. Due to lack of continuous conventional cores at Site NGHP-02-16, gas hydrate related insights from physical property characteristics are only reviewed for Sites NGHP-02-17 and −23.

The lithological unit boundary depths shown in Fig. 3, which are defined based on shipboard visual core descriptions, are reproduced on the downhole LWD and sediment property logs in Fig. 4. These unit boundary depths correlate well with changes in downhole physical properties. Starting with the lowest unit (Unit V) and working toward the seafloor, the following observations can be made for the anticline crest region.

Below the Unit IV reservoir section, Unit V at NGHP-02-17 (> 313.1mbsf) and NGHP-02-23 (> 299.6mbsf) is considered as an underlying sediment layer with lower sand content than is in the reservoir Unit IV (e.g., in Fig. 4 b and c, natural gamma radiation, sediment component content and grain size panels). The anticline core itself is considered to be dominated by Miocene shales (Shukla et al., 2019-b). The top of Unit V is below the base of observed gas hydrate occurrence and the estimated BSR depth (Table 1).

In most cases along the crest of the anticline, Unit IV contains pore-filling gas hydrates at high saturations (Fig. 4-a, b and c). However, along the flanks of the anticline, the coarse-grained reservoir layers in Unit IV extend below the base of observed gas hydrate stability zone (Table 1). Based on caliper logs showing borehole washouts (Waite et al., 2019-a), and acoustic logs (Collett et al. 2019) these extensions below the base of observed gas hydrate appear to be water-saturated. Core-derived porosity measurements in these water-saturated, coarse-grained sediments are more reliable than the LWD results since these water-bearing layers are weak enough to be washed out during logging (e.g., for NGHP-02-17 at 294mbsf, the core-derived porosity of 43% is less than the 62% porosity calculated from LWD data).

Seismic profiles (Fig. 2a, b and c) indicate the R2 reflector at the top of Unit IV is the only significant acoustic impedance contrast along the crest of the anticline. This observation is compatible with LWD measurements of bulk density and V_P, which both vary relatively smoothly downhole until ~271mbsf where both properties dramatically increase. The Unit IV gas hydrate-bearing reservoir section from the top (~273mbsf) to the bottom at Site NGHP-02-16 (296mbsf), Site NGHP-02-17 (313.1mbsf) and Site NGHP-02-23 (299.6mbsf) is characterized by lower porosity values and higher V_P than the adjacent Units III and V. Unit IV can also be distinguished by relatively high values in the natural gamma ray, resistivity and QFM log data (Fig. 4a, b and c).

In Unit IV, the clay content is low, meaning the packing conditions of bulky sandy grains govern the reservoir sediment fabric, which causes a porosity drop from about 70% at the base of Unit III to 40% in Unit IV (Fig. 4a, b and c). For comparison, the porosity of F110 sand has been noted in other studies to be between 35 and 46% (Cho et al., 2006). Though porosity and water content are relatively low in Unit IV relative to Units III and V, the low clay content and coarser grains produce larger pore sizes that are more conducive to hosting gas hydrate (e.g. Kraemer et al., 2000; Torres et al., 2008; Uchida et al., 2009). Accordingly, pore-filling gas hydrate occurs in Unit IV. As shown by the gas hydrate saturation trend, S_H (Collett et al., 2019), in Fig. 4b and c, the upper portion of Unit IV tends to be more fully saturated than the lower portion since gas hydrate saturation in part reflects the balance between sand and clay concentrations (Fig. 4 b, c; QFM-clay profiles: note general increase in clay content with depth in Unit IV). Although the lower portion of Unit IV has higher clay content than the upper portion, this section is still coarse enough to behave as an uncemented, water-bearing sand with washouts, observed during drilling in this interval.

Along the anticline crest, Unit III extends upward from the top of Unit IV, contacting either Unit I (NGHP-02-17 near 173mbsf) or Unit II (NGHP-02-23 near 181mbsf) as indicated for NGHP-02-17 and −23 in Fig. 3. In Unit III, the porosity increases with depth, reaching just above 70% at the top of Unit IV. Over this depth range, the concentrations of micro- and nannofossils such as diatoms also increase, which affects the downhole porosity, grain density and water content profiles. Diatoms, with their low grain density (1.4–2.2 g/cm^3 (Miklasz and Denny, 2010; Wiemer et al., 2017)), inner porosity, and rough structure (Fig. 5f), can generate high overall sediment porosity, low grain density, and high water content. For example, in Fig. 4b for NGHP-02-17, at a depth of 254.59mbsf, the porosity is 76.34%, with a 2.45 g/cm^3 grain density and 1.346 water content. The effects of diatoms on the porosity profile have also been observed in other marine settings (Kraemer et al., 2000; Spinelli et al., 2007).

Along the anticline crest, the high-porosity, diatom-rich qualities of Unit III enhance the unit's permeability and contribute to this layer's inability to seal methane into the coarse-grained sediment layers in the underlying Unit IV. A second factor degrading the Unit III sealing capabilities is the near-vertical faults that penetrate and potentially compartmentalize the Area B reservoir system at the anticline crest (Collett et al., 2019; Saito et al., 2019; Shukla et al., 2019-b). Whether directly through Unit III sediment or along the available faults, methane migrates out of Unit IV through a thin interval of slightly elevated clay content in Unit III (Fig. 4b and c) and forms gas hydrate within the upper part of Unit III.

The lack of gas hydrate near the base of Unit III in spite of the bounding gas hydrate present in the upper portions of Unit III and IV is likely related to a localized shift in the methane solubility limit. As described by Henry et al. (1999), the methane solubility limit, which dissolved phase methane concentrations must exceed before gas hydrate can form, increases with decreasing pore size. In spite of the elevated porosity at the base of Unit III, the fine-grained nature of Unit III related to Unit IV means gas hydrate formation in Unit III requires a higher methane concentration than exists in equilibrium with the Unit IV gas hydrate. As shown by Xu and Ruppel (1999), the solubility requirement decreases as the dissolved-phase methane migrates upward into cooler sediment. Once the methane has migrated upward into Unit III far enough for the solubility limit in the cool, fine-grained, small-pore sediment to fall below the solubility limit in the warm, coarse-grained, large-pore Unit IV sediment, gas hydrate can begin forming. Gas hydrate saturation in the upper portion of Unit III fluctuates on small spatial scales as the proportions of clay and sand vary with depth, and as inferred by Collett et al. (2019), many of the observed gas hydrate-bearing fractures in Unit III are linked with thin, sand-rich layers that also host gas hydrate.

Unit II thins out near the anticline crest, becoming difficult to distinguish (Fig. 3). Unit II is observed more readily away from the anticline crest (e.g. NGHP-02-19, −22- and −23, Fig. 3), indicating this unit was deposited after the deformation that created the anticline (Saito et al., 2019). Unit II is discussed in greater detail for NGHP-02-22 and −19, where it is thicker and better characterized (Sections 4.2 and 4.3).

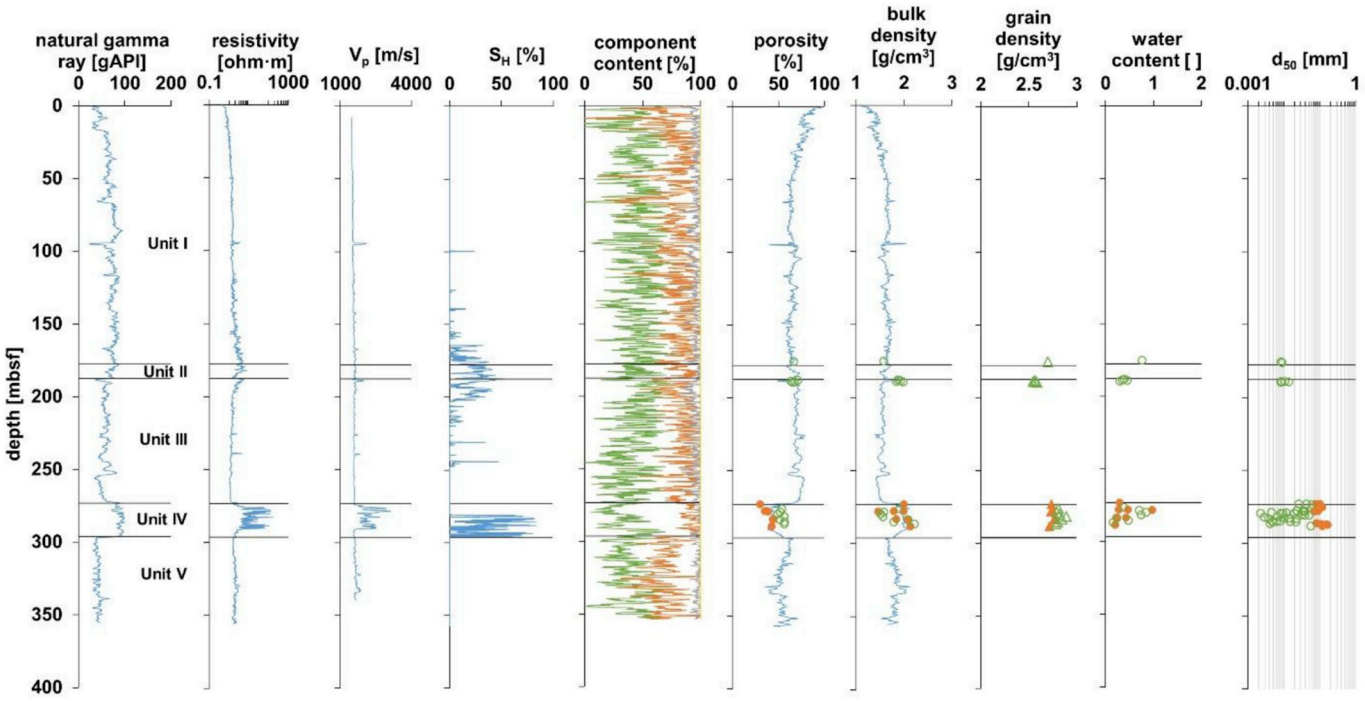

(a) Site NGHP-02-16

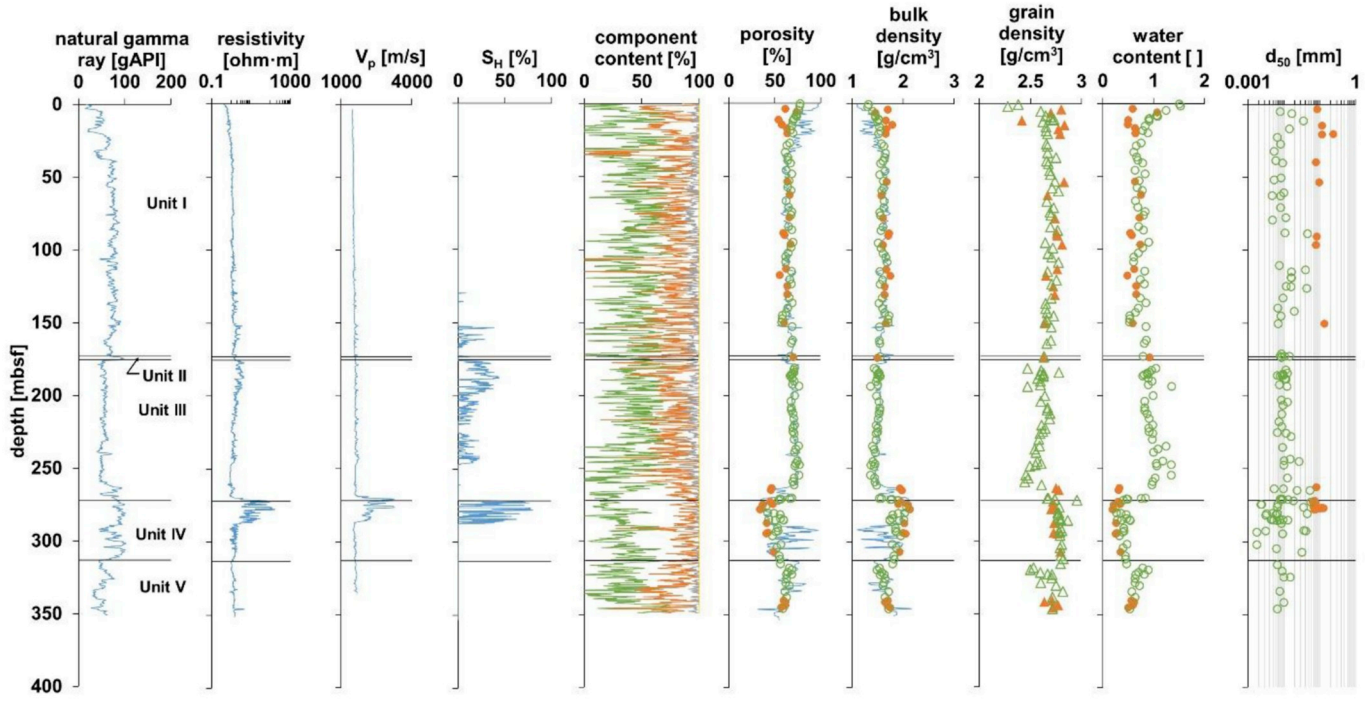

(b) Site NGHP-02-17

Fig. 4. The profiles of porosity, grain density, dry water content, grain size of d_{10}, d_{50} and d_{90} and the clay content at (a) Site NGHP-02-16, (b) NGHP-02-17, (c) NGHP-02-23, (d) NGHP-02-22 and (e) NGHP-02-19. Continuous line data is from LWD and discrete data are from core measurements. Site NGHP-02-22 coring extended more deeply than the LWD measurements (Legend – in Component Content, green line: clay; orange line: QFM; grey line: calcite; gold line: pyrite (Note: The sequence of concentrations are cumulative, so pyrite curve is at 1 because it represents clay + QFM + calcite + pyrite); in porosity, bulk density, grain density, water content and d_{50}, continuous line: LWD data, solid circle: sandy sediment, empty circle: mud). (For interpretation of the references to color in this figure legend, the reader is referred to the Web version of this article.)

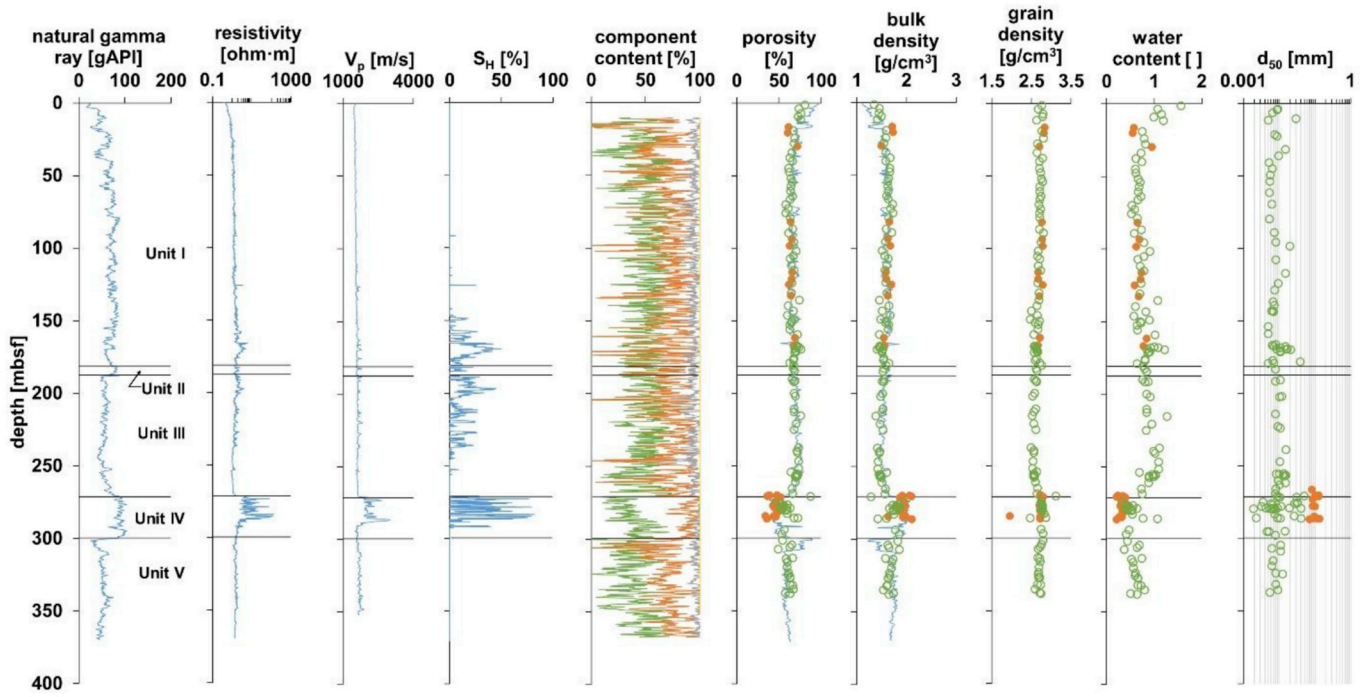

(c) Site NGHP-02-23

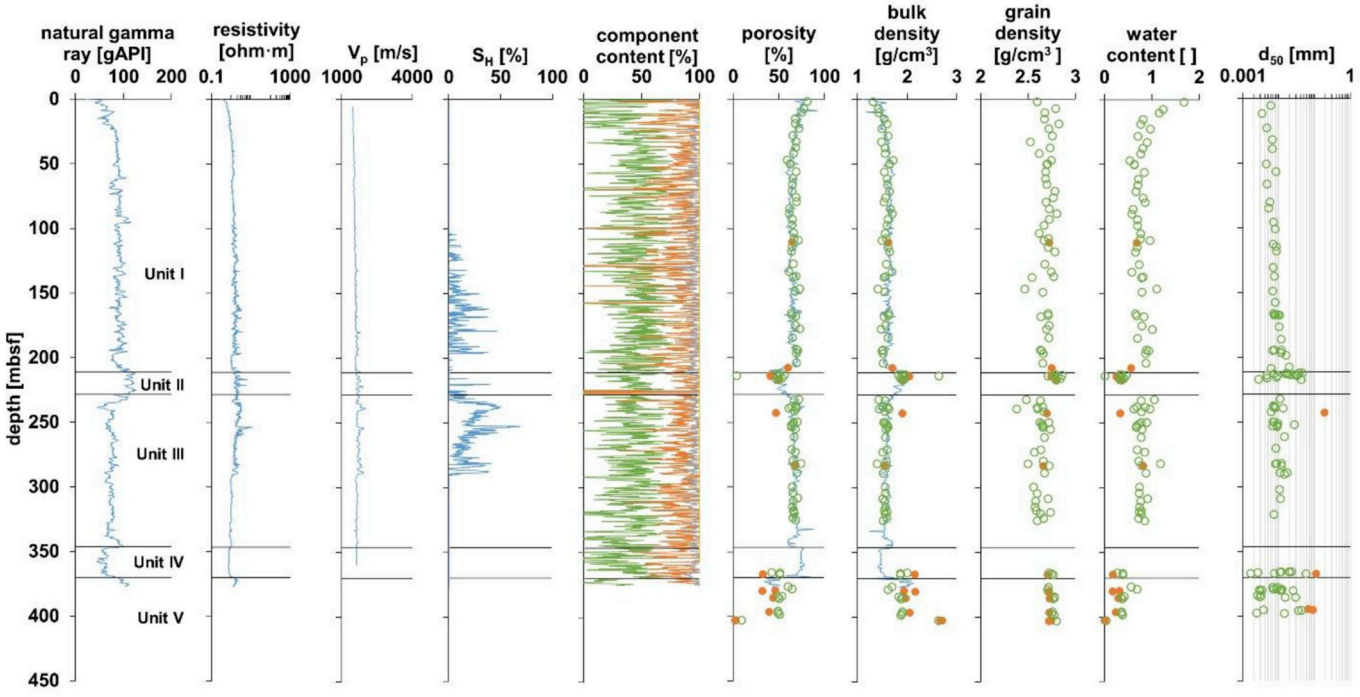

(d) Site NGHP-02-22

Fig. 4. (*continued*)

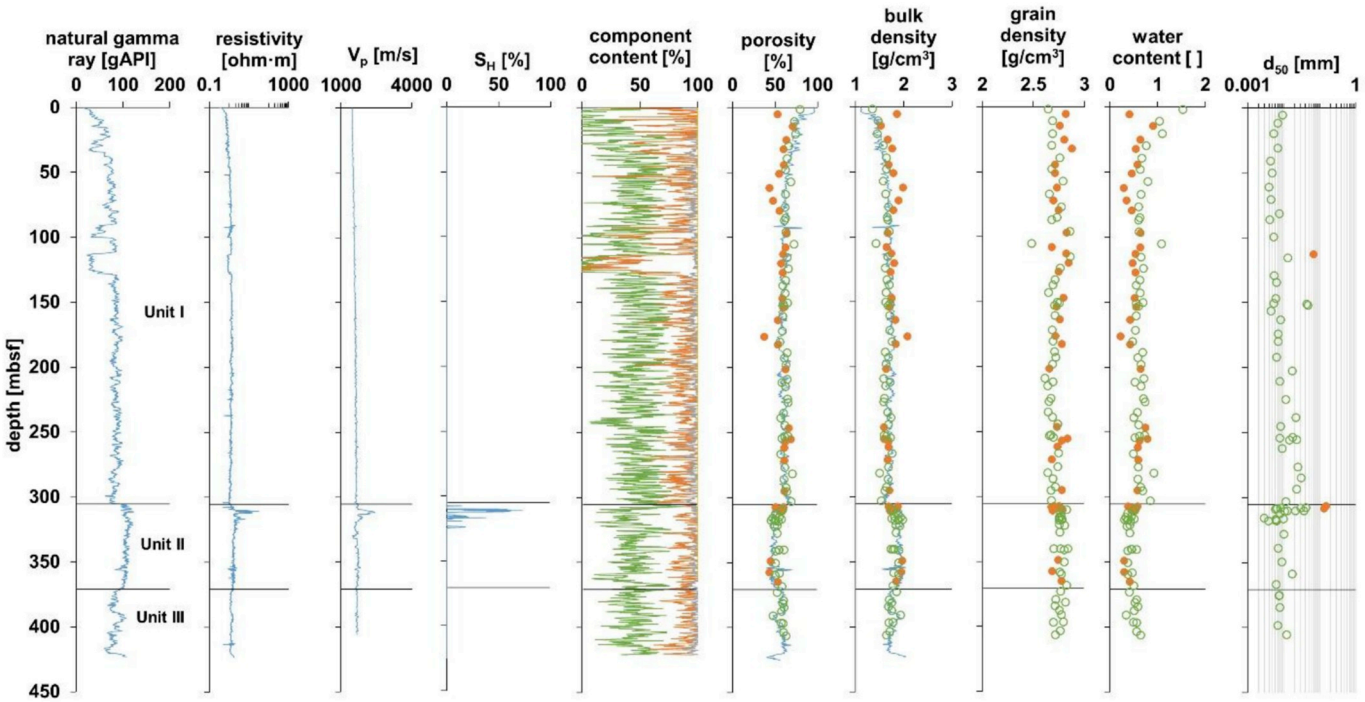

(e) Site NGHP-02-19

Fig. 4. (*continued*)

Unit I hosts gas hydrate-filled fractures primarily in the lower portion, near the depth where Unit II thins (Fig. 4). Unit I appears to be the primary seal near the crest of the anticline, restricting gas hydrate growth to depths below ~150mbsf. Relative to Unit III, Unit I may be a more effective seal because of slight variations in the porosity and grain size with depth. Unit I porosity decreases from 80% near the seafloor to ~63% at 50 mbsf, as anticipated for sediments compacting normally with depth. Between the 50mbsf and the bottom of Unit I, however, the porosity increases slightly with depth (e.g. NGHP-02-17, Fig. 4b). Additionally, the grain size increases slightly with depth (e.g. d_{50} at NGHP-02-17, Fig. 4b), though the grain size is more variable at shallow depths. A third consideration for the Unit I seal quality is the lower concentration of micro- and nannofossils and correspondingly lower permeability in Unit I relative to Unit III.

A fourth consideration for the Unit I seal quality, unrelated to the Unit I sediment characteristics, is the upper extent of the faults that extend upward through the Unit IV reservoir, penetrating into Unit I. A fault near NGHP-02-23 appears to end in Unit I near the NGHP-02-23 top of gas hydrate at 150mbsf. Other faults appear to terminate near ~150mbsf as well. Above this depth, Unit I appears to be free of vertical faulting, and free of gas hydrate-filled fractures (Saito et al., 2019).

At the anticline crest, the most effective barriers to the upward migration of methane are in Unit I, and not in direct contact with Unit IV, the primary gas hydrate reservoir. The seal layer directly above Unit IV at the anticline crest is imperfect, allowing upward fluid flow that can transport dissolved-phase methane out of the reservoir and into the overburden. Because the overburden is cooler than Unit IV, the methane solubility requirement in the overburden is lower than in Unit IV and hydrate can form with smaller pore-water methane concentrations than are required to maintain gas hydrate in Unit IV (e.g. Xu and Ruppel, 1999).

In terms of the modified gas hydrate petroleum system approach, the “effective methane seal” at the anticline crest, which accounts for the rate of methane loss in relation to the rate of methane supply, does not slow the pore-fluid flow enough for microbial methane production to yield high enough methane concentrations to fill Unit IV top-to-bottom with gas hydrate. As noted by Collett et al. (2019) and Waite et al. (2019a,b), Unit IV contains water-bearing, relatively coarse-grained sediments in contact with the primary gas hydrate-hosting sediment.

4.2. Anticline slope: site NGHP-02-22

As shown in the seismic lines in Fig. 2a and b, holes drilled and cored from several sites penetrate the R1 and R2 reflectors, as well as the BSR. The relative strengths and depths of these reflectors are associated with the distribution of gas hydrate occurrences at this site. At NGHP-02-22, R1 is located above the BSR, within the gas hydrate stability field, and is not much stronger than R2. The R1 reflector at this site is the same phase (normal polarity) as the sea floor reflection and the R1 peak/trough pair is inferred to span only a few meters more than the thickness of Unit II, which is encompassed by R1 at this site (Table 1). As the polarity indicates, Unit II is more dense (lower density porosity, ϕ_D, Eq. (1)) and has a higher V_p than the overlying Unit I, but the V_p increase is slight, and Unit II hosts only limited gas hydrate saturation (Fig. 4). Consequently, the R1 reflector at NGHP-02-22 is muted relative to the R2 reflection near the anticline crest.

Shukla et al. (2019-b) notes the phase of the R2 reflector where it lays just above the BSR at the crest of the anticline has the same polarity as the seafloor, as expected given the increased formation density and V_p of Unit IV relative to the overlying Unit III (Figs. 2a and 4b, c). Along the flank of the Area-B anticline, where the R2 reflector occurs below the BSR (the assumed base of gas hydrate stability in this region), the phase of the R2 reflector appears to still have the same phase as the seafloor reflection, indicating the continued high formation density of Unit IV relative to the overlying Unit III section as measured by LWD (Fig. 4d).

Unit IV is below the base of gas hydrate occurrence at Site NGHP-02-22. Physical property characteristics in Unit IV below the BSR are similar to those measured for Unit IV at the anticline crest: low porosity,

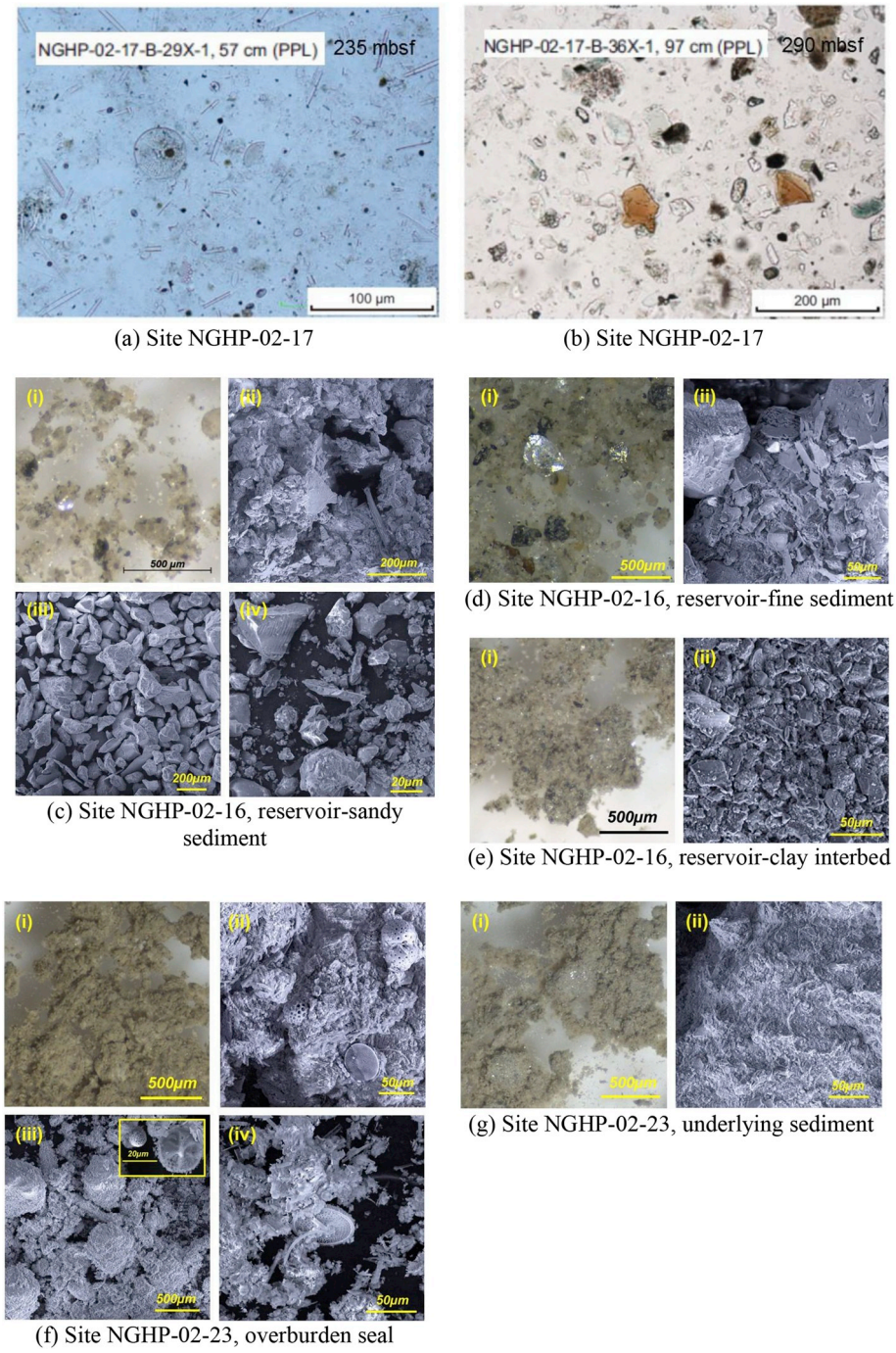

Fig. 5. Microscope images of (a) diatoms in Unit III at Site NGHP-02-17 and (b) quartz particles in Unit IV in Site NGHP-02-17 from shipboard smear slide data; the five samples from Table 2 are imaged in c–d: (c) reservoir-sandy interbed, (d) reservoir-fine sand, (e) reservoir-clay interbed, (f) overburden seal and (g) underlying sediment. (Legend – i: stereotype microscope, whole sample image, ii: SEM, whole sample image, iii: SEM, coarse grains after dry sieving, iv: SEM, fine grains after dry sieving).

high grain density and low water content (compare Fig. 4c and d). Below the base of gas hydrate stability, the relatively coarse-grained nature of Unit IV relative to the adjacent units likely allows Unit IV to act as a conduit for methane to migrate into the primary gas hydrate reservoir near the anticline crest (Collett et al., 2019; Saito et al., 2019).

Unlike Unit IV, the upper portion of Unit III (265mbsf to 228.4mbsf) contains fines with appreciable concentrations of diatoms, as it does along the anticline crest. As can be seen in the downhole grain size profile, thin, coarser-grained layers do exist in Unit III (~240mbsf), but the unit contains mostly fine-grained sediment (Fig. 4). The gas hydrate saturation in Unit III generally decreases with depth. At the BSR depth of ~290mbsf, there is not a dramatic contrast in bulk density (or porosity in Fig. 4), and V_p drops only from ~1900 m/s to 1600 m/s around 290mbsf. A nearly constant density, combined with a small velocity drop, is consistent with a small impedance contrast and hence, a weak BSR at the base of gas hydrate stability (Fig. 2c; details in Waite et al., 2019-a).

Unit II, which thickens downslope and is ~20 m-thick at NGHP-02-22 (Table 1), is defined by elevated natural gamma ray, QFM and grain size values (Fig. 4d). Though this response is analogous to the Unit IV response at the anticline crest, Unit II does not appear to host significant gas hydrate saturations (Collett et al., 2019). Unit II may instead

Table 3
Particle sizes of sandy layers from collected cores (the site number is listed as NGHP-02-xx).

Site No.	depth [mbsf]	sand %	particle sizes [mm]					C_u
			d_{10}	d_{30}	d_{50}	d_{60}	d_{90}	
NGHP-02-16	273.23	53.3	0.0051	0.028	0.0804	0.101	0.2782	19.7
	273.23	60.6	0.0092	0.0401	0.1045	0.11	0.3317	12.0
	275.50	69.6	0.0119	0.06	0.1212	0.11	0.2543	9.2
	275.50	72.6	0.0145	0.07	0.1155	0.13	0.2690	9.0
	278.22	60.7	0.0107	0.041	0.0903	0.101	0.3067	9.4
	286.50	56.1	0.0085	0.039	0.0815	0.1	0.2389	11.8
	286.50	59.7	0.0096	0.041	0.0850	0.101	0.3258	10.5
	287.34	66.3	0.0088	0.06	0.1579	0.19	0.3965	21.5
	287.37	65.5	0.0085	0.06	0.1688	0.2	0.4284	23.5
	288.43	72.3	0.0143	0.07	0.1203	0.13	0.3191	9.1
NGHP-02-17	262.79	58.7	0.0100	0.04	0.0817	0.09	0.1946	9.0
	272.05	53.7	0.0052	0.031	0.0697	0.09	0.2410	17.3
	272.19	56.0	0.0063	0.031	0.0739	0.09	0.2011	14.3
	272.85	56.4	0.0049	0.031	0.0757	0.09	0.0757	18.4
	272.91	50.9	0.0040	0.024	0.0650	0.08	0.1815	19.9
	274.86	55.0	0.0095	0.04	0.0705	0.09	0.2336	9.5
	274.89	57.8	0.0144	0.042	0.0811	0.091	0.2280	6.3
	276.80	50.4	0.0060	0.0301	0.0697	0.08	0.2226	13.2
	276.93	69.2	0.0240	0.061	0.1134	0.11	0.2787	4.6
	276.99	74.1	0.0291	0.071	0.1307	0.12	0.3021	4.1
	277.15	71.4	0.0201	0.065	0.1141	0.12	0.2931	6.0
	277.27	70.2	0.0187	0.064	0.1044	0.11	0.3001	5.9
	278.01	60.2	0.0194	0.042	0.0799	0.091	0.1904	4.7
	278.03	57.4	0.0166	0.045	0.0730	0.09	0.2163	5.4
NGHP-02-19	306.55	52.1	0.0035	0.024	0.1546	0.19	0.5146	54.2
	308.56	60.5	0.0025	0.013	0.1353	0.104	0.2916	41.4
NGHP-02-22	242.84	81.8	0.0188	0.101	0.1931	0.11	0.4193	5.8
NGHP-02-23	270.06	68.6	0.0116	0.061	0.1282	0.104	0.3110	9.0
	270.34	68.3	0.0094	0.06	0.1063	0.11	0.2920	11.7
	270.86	66.0	0.0088	0.051	0.1304	0.104	0.3293	11.8
	277.69	54.7	0.0113	0.038	0.0875	0.101	0.2830	8.9
	277.99	61.2	0.0067	0.044	0.1022	0.101	0.2444	15.1
	284.67	65.8	0.0173	0.051	0.0982	0.101	0.2202	5.8
	286.16	68.8	0.0195	0.06	0.0926	0.102	0.2082	5.2
	286.50	72.8	0.0208	0.07	0.1361	0.104	0.3119	5.0
	286.50	74.1	0.0197	0.071	0.1202	0.14	0.3052	7.1
	286.71	50.4	0.0039	0.021	0.0720	0.1	0.2541	25.3

Remarks.
No gravel-size particles.
Assumed roundness, R = 0.2.
Assumed liquid limit = 50.
$C_u = d_{60}/d_{10}$.

provide a relatively permeable conduit for methane to migrate toward the anticline crest, similar to Unit IV (Saito et al., 2019). Since there is no independent verification of the Unit II permeability, this inference has not yet been completely confirmed (Collett et al., 2019). Above Unit II, LWD and core analyses show trends in the fine-grained overburden of Unit I at Site NGHP-02-22 are consistent with the other sites in Area B.

4.3. Anticlinal flank: site NGHP-02-19

As shown Fig. 2b, Site NGHP-02-19 is located in a syncline northeast of the anticline crest. As indicated in Fig. 2, the reflector R1 observed starting at ~207mbsf at Site NGHP-02-22 has dipped along with the Unit I/II transition to ~305mbsf at Site NGHP-02-19. At NGHP-02-19, R1 lies just above the BSR and is fairly strong, consistent with the increase in bulk density (porosity decrease), V_p and S_H near this depth.

At Site NGHP-02-19, Unit III is the deepest unit penetrated, constituting mud layer containing microfossils and nannofossils at the base of the hole. Unit II extends from its contact with Unit III at 370.7mbsf to 305mbsf. As observed at NGHP-02-22, Unit II can be characterized by elevated gamma ray values, high QFM content, low porosity and low water content relative to the adjacent Units I and III. Gas hydrate that has concentrated in Unit II is localized the near the upper contact of Unit II with Unit I. The top portion of this occurrence is associated with a thin, coarse-grained unit that corresponds with the upper bound of a bright resistivity band (Fig. 3). The lack of gas hydrate in Unit II is consistent with the Unit II serving primarily as a conduit for methane migration up the anticline flank (Saito et al., 2019), but this interpretation would be more certain if the Unit II permeability were known, and shown to be higher than that in Unit's I and III (Collett et al., 2019). The restricted gas hydrate distribution at NGHP-02-19 suggests the methane supply is limited at this site relative to both the methane loss occurring along Unit II toward the anticline crest, and the methane bleeding vertically into Unit I.

Unit I is thicker at NGHP-02-19 than at other sites on the anticline crest and slope and can be divided into three subunits: IA, IB and IC. Subunit IC (182-305mbsf) has intervals of alternating beds of silty clay and fine sand. Subunit IB (132-182mbsf) contains abundant MTD with nannofossils and microfossils, and Subunit IA (0-132mbsf) is composed of pelagic silty clay with thin silty layers.

5. Lab-characterization of sediments: results and analysis

Table 2 summarizes the physical property data for the five anticline crest samples selected for additional geotechnical testing, with a particular focus on how these sediments are likely to respond to the effective stress increase and pore water freshening that occur when methane is extracted via depressurization during gas production. Samples were recovered to further characterize the reservoir overburden, the reservoir itself, and the underlying sediment. Within the reservoir, three distinct samples were collected covering a range of sand and clay contents to investigate the properties of the coarse-grained reservoir layers, the fine-grained interbeds, and the transitions between these two reservoir endmembers. For additional site context, results from these five samples are also assessed in combination with shipboard measurements and downhole LWD data.

5.1. Grain size distribution

Fig. 4 provides downhole profiles of d_{50}, the median grain size, as a representative particle size. The distribution full grain size profiles (Waite et al., 2018 c) show that most of the analyzed samples contain muddy sediments, defined as $d_{50} < 63\,\mu m$. Keeping in mind that Area B is more than 150 km northeast of the NGHP-01 well locations in the Krishna-Godavari Basin (Fig. 1a), the d_{50} grain sizes for the fine-grained sediment in Area B is comparable to the observed d_{50} for NGHP-01 fines. Winters et al. (2014) report median grain sizes of 5 ~ 7 μm for the Krishna-Godavari Basin fines tested along the upper continental slope sites (NGHP-01). In Area B, which tests lower continental slope sediment, the median size of the fines is ~10 μm (Fig. 4).

Those samples with $d_{50} > 63\,\mu m$ are summarized in Table 3, including all samples taken from the sandy reservoir layers from Unit IV the anticline crest. Characterized solely by size, the samples in Table 3 would not be classified as “fines,” but this study reassesses the sandy sediments using the revised soil classification system (RSCS) for coarse-fine mixtures (Park and Santamarina, 2017). The RSCS utilizes particle size information, particle shape and liquid limit data to identify whether the fine or coarse grains in the mixture control mechanical properties such as shear strength and fluid flow properties such as permeability. Table 3 provides the parameters required to classify the sediments. The particle roundness has been estimated from SEM images and a particle shape chart (Cho et al., 2006), and the liquid limit is taken to be 50 (see also Table 2) as a conservative estimate that tends to drive the classification in the direction of coarse sediment. RSCS results show that all sediments in Table 3, which would be classified as sandy

based solely on particle size, are classified as F(F) using the RSCS approach. This means fines are expected to control both the mechanical and flow properties of these "sandy" sediments. This classification result highlights the importance of characterizing the types of fines that are present at any site and measuring how fines respond to the mechanical and pore-fluid chemistry changes occurring during the extraction of methane from gas hydrate as an energy resource. Laboratory experiments in this study are designed to characterize the fines, constrain the behavior of fines during gas extraction, and provide insight into the potential productivity of the primary Area B gas hydrate reservoir on the anticline crest.

5.2. Microscope images

Based on stereotype microscope and SEM images, we can see differences between the coarse and fine grains of quartz, mica, clay minerals and microfossils (diatoms). The coarse-grained fraction is observed as clean, individual particles in microscope and SEM imagery (Fig. 5c–i and 5d-i). In addition, stereotype microscope images show how fines can be distinguished on the basis of distinct clustering behaviors. For instance, one type of fines (smectite) can attach onto coarse grains due to electrical inter-particle forces at ambient atmospheric conditions (e.g. Jang et al., 2018a). At these dry conditions, the bulky larger grains become coated in clusters of fine particles and look fluffy (Fig. 5 e, f and g). A second type of fines (e.g. small quartz particles) remains separated from the individual particles of bulky, angular grains: they are distinguishable even under the stereotype microscope. These fines do not appear to cluster (Fig. 5c and d). Fig. 5f provides images of the overburden seal, made up of coarse grains coated by fines and microfossils. In particular, at the concentrations found in Unit III, microfossils such as diatoms can control sediment characteristics and noticeably affect LWD measurements and downhole sediment property profiles. In addition, pyrite framboids (inset of Fig. 5f–iii) could be an indicator of past methane oxidation or sulfate reduction by microbial activity (Musgrave et al., 2006).

5.3. XRD

Table 4 contains the XRD mineralogy distribution for the five specimens described in Table 2. As expected, the reservoir layer has a higher quartz content than the fine interbeds and seal layers. The seal layers have higher illite content than the reservoir sediments. Recognizing that certain fines, such as illite and smectites can be difficult to identify and quantify using XRD, this study utilizes electrical sensitivity tests and sedimentation tests (both explained below) to assist in the fines characterization. Although the analyses are not carried out on precisely the same material, the XRD results are also compared to shipboard smear slide data, which can identify certain sediment components such as diatoms, more readily than XRD. In each case, the nearest smear slide specimen is taken ($\sim$0.1–2 m away from the sample) from the same lithology as the XRD sample.

5.4. Specific surface

Specific surface measurements aid the interpretation of LWD data on mineralogy and porosity, which are related to the mud content. The specific surface generally increases when the mud content in a specimen increases (Table 2). For example, fine sand in the reservoir unit has the lowest specific surface value and the lowest mud content. Mud content in the overburden seal specimen is less than what is observed in the underlying sediment specimen, but the specific surface of the overburden seal specimen is greater than that of the underlying sediment specimen because of diatoms in the overburden. Because of their internal porosity, diatoms have a high specific surface, $\sim$100 m^2/g. The presence of diatoms in the overburden seal is confirmed by SEM, XRD pattern shape, and smear slide results.

5.5. Electrical sensitivity

The as-recovered, unconfined disturbed marine sediments were first dried, which allowed salt in the in-situ pore fluid to precipitate onto the sediment. That salt may affect the liquid limit measured in deionized water because the salt can dissolve, adding ions to the deionized water. This can alter the sediment fabric, and hence, the measured liquid limit.

Table 4
X-ray-diffraction and smear-slide results for the five Area B specimens described in Table 2, showing the percent (by mass) of the sediment components. The first three components, quartz, feldspar and mica, combine to approximate the QFM result from LWD. Smear slide results provide an independent assessment of the XRD pattern interpretation.

Specimen Environment	reservoir- fine sand (Coarse)	reservoir-sandy interbed (Coarse and fine)	reservoir-clay interbed (Fine)	overburden seal (Fine)	underlying sediment (Fine)
Specimen ID	633170	640170	634470	585170	590470
Depth (mbsf)	278.2	278.0	285.6	262.6	295.2
Material	(%)	(%)	(%)	(%)	(%)
Quartz	47.1	39.6	29.4	13.2	27.8
Feldspar	18.8	21.9	24.6	20.6	16.5
Mica	11.5	15.7	25.4	18.9	32
Carbonate	8.5	14.3	6.3	7.6	1.2
Chlorite	6.2	4	10	10.2	3.59
Illite	3.5	4.6	3.5	29	19.3
Hornblende	4.3	0	1.17	0	0
Sulfides	0	0	0	0.8	0
Smear Slide Comparison	636070	635970	636270	586670	593970
Quartz	89	74	9	3	9.6
Carbonate			30		
Carbonate Mud					25
Carbonate Silt		18			
Clay				30	25
Microfossils				22	
Mudstone			46		
Pyrite				3	
Smear slide designation	Quartz-rich sand	Quartz-rich silt	Silty clay	Diatom-bearing, mudstone-grain-rich clayey silt	Carbonate-rich clay

The liquid limit for the original dry specimen with deionized water is 77. After the dilution process, the liquid limit with deionized water drops to 61. The reduction may be due to drying process in sample preparation. Also, some fines in the supernatant during the dilution process could have been siphoned off and lost, which would reduce the liquid limit. Thus, sample preparation may offset the effect of the pore-fluid chemistry, ionic concentration, and permittivity change for the liquid limit using 2M-brine (LL_{brine} = 53) and kerosene (LL_{ker} = 46). Based on the fines classification with electrical sensitivity, the sediment is inferred to be intermediate plasticity fine grains of low electrical sensitivity (Jang and Santamarina, 2016, 2017). However, a higher value in the electrical sensitivity (> 0.4) is anticipated when there is enough sample to complete all three liquid limit tests without reusing sediment.

5.6. Sedimentation test

Fig. 6a shows a schematic of the sedimentation test, including definitions of the interface heights that are tracked over time. The depositional height is the height of the falling interface between the supernatant and the cloudy suspension. The accumulated height is the height of the rising interface, and mainly tracks the settling of gravimetric-dominated particles to the bottom of the sedimentation cylinder (Fig. 6a). In considering the sedimentation tests, four test aspects are significant for establishing how the sediment fabric depends on pore-fluid chemistry: sedimentation behavior (segregated versus uniform), supernatant turbidity, depositional interface falling velocity, and final sedimentation height.

The most significant sedimentation test aspect to track is the sedimentation behavior itself. Segregated sedimentation occurs when the finer grains remain suspended well after the coarser grains have settled out. This behavior is generally associated with a distinguishable, rising accumulated interface and turbid supernatant. Unlike segregated sedimentation, uniform sedimentation does not occur with two distinguishable interfaces. Only the depositional interface is distinguishable as it falls, and the supernatant above the depositional interface tends to be clear.

Sedimentation test results indicate how interparticle interactions change as a function of the pore-fluid chemistry, and illustrate how those interaction changes alter the sedimentation pattern and affect the void ratio of the resulting sediment fabric. The freshened water (DWF), dissolved salt water (DWS) and 2M-brine show segregated sedimentation, but all sedimentation in kerosene is uniform. The sedimentation heights are shown in Fig. 6b and f, and descriptions of the interface visibility and supernatant turbidity are given in Table 5. The interface falling velocities are presented in terms of t_{50}, the time required for the interface to move halfway between its initial and final height, in Fig. 6g. The final interface heights, which indicate sediment fabric and packing conditions, are given relative to the initial 25.4 mm dry specimen height in Fig. 6h. The data plotted in Fig. 6 are available for download from Jang et al. (2018c).

5.6.1. Reservoir-fine sand (633170)

Particles segregate in DWF, DWS, and 2M-brine as the larger, gravimetric-dominated particles stack on the bottom to form the accumulation interface. The depositional height is not distinct and the supernatant above the accumulation interface is cloudy until the end of the tests in DWF and DWS. Based on XRD and SEM results, the fine particles are mainly bulky and angular quartz. Due to repulsive electrical forces between these types of particles, fines in DWF and DWS do

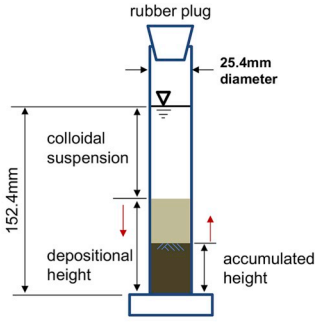

(a) Experimental schematic

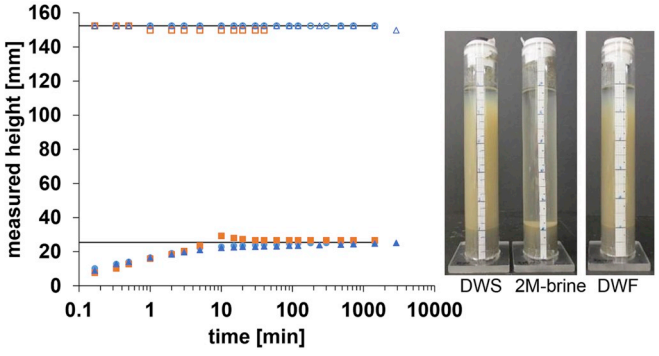

(b) Reservoir-fine sand

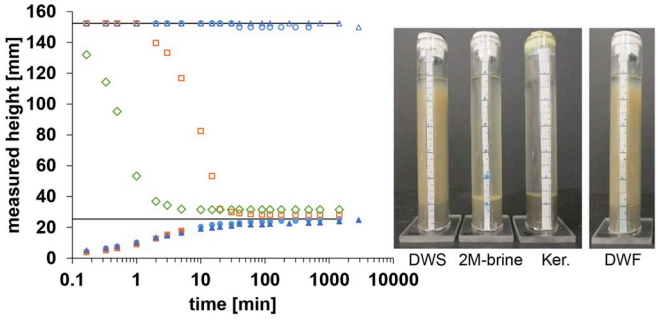

(c) Reservoir-sandy interbed sediment

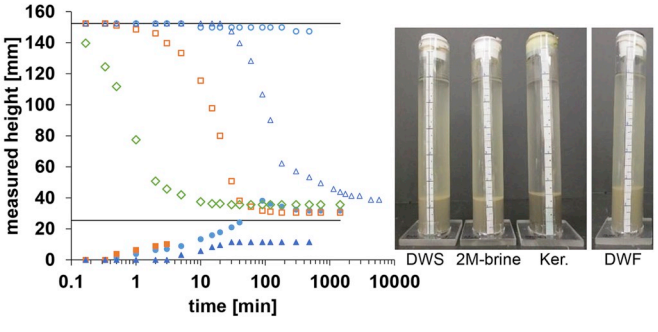

(d) Reservoir-clay interbed

Fig. 6. Sedimentation tests: (a) experimental configuration and description of the depositional and accumulated height; Measured sedimentation heights and images at final status of (b) reservoir-fine sand, (c) reservoir-sandy interbed, (d) reservoir-clay interbed, (e) overburden seal and (f) underlying sediment; (g) the falling time at half-way to final height, (h) the ratio of final height to 25.4 mm. Legend – triangle: freshened water (DWF), circle: dissolved salt water (DWS), square: 2M-brine, diamond: kerosene (Ker), the solid symbols represent the accumulated height and empty symbols the depositional height. Fluid name abbreviations below each settling cylinder image indicate the test fluid for that cylinder.

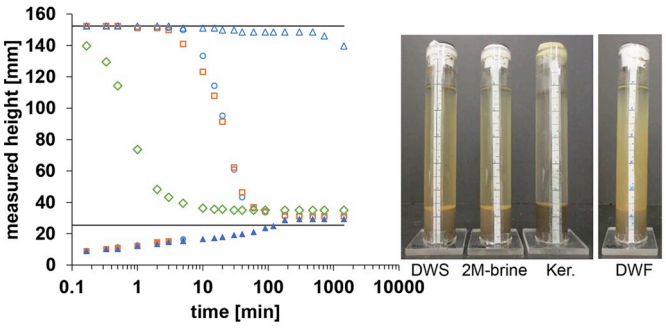

(e) Overburden seal

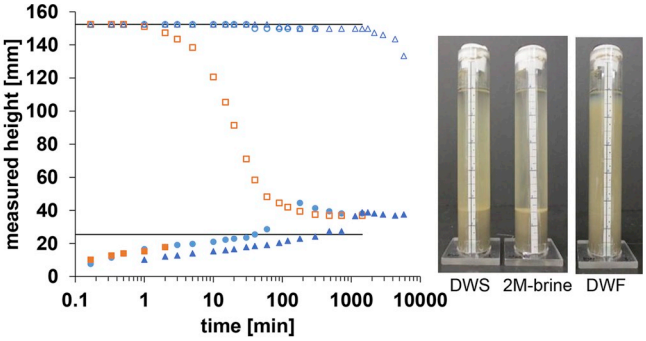

(f) Underlying sediment

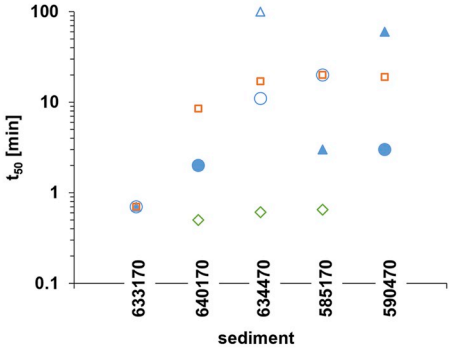

(g) Interface falling time

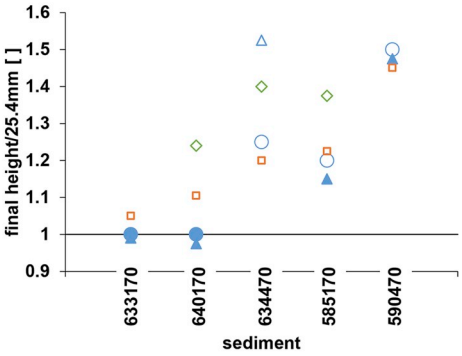

(h) Normalized final interface height

Fig. 6. (*continued*)

not cluster. However, the additional salt in 2M-brine increases the ionic content of the water and helps these fines cluster and settle more rapidly (Sogami and Ise, 1984; McBride and Baveye, 2002). Thus, the falling velocity for fines in 2M-brine is much faster than in DWF and DWS. The falling velocities of the gravimetric-dominated particles in the three fluids are similar though. The final accumulated interface heights at the end of the tests in DWF and DWS are slightly less than 25.4 mm because the fines remain largely suspended and do not

Table 5
Description of the sedimentation test characteristics. For each sample, the salinity increases in the order DWF < DWS < 2M-brine.

Sample ID	fluid	supernatant turbidity	interfaces	
			depositional	accumulated
reservoir-fine sand (633170)	DWF	turbid	not-distinguishable	distinguishable
	DWS	turbid	not-distinguishable	distinguishable
	2M-brine	become clear	not-distinguishable	distinguishable
	kerosene	N/A	N/A	N/A
reservoir-sandy interbed (640170)	DWF	turbid	not-distinguishable	distinguishable
	DWS	turbid	not-distinguishable	distinguishable
	2M-brine	become clear	blurry	transitional[1)]
	kerosene	clear	obvious	not-distinguishable
reservoir-clay interbed (634470)	DWF	become clear	distinguishable	transitional
	DWS	become clear	not-distinguishable	intermittently distinguishable[2)]
	2M-brine	become clear	distinguishable	transitional
	kerosene	clear	obvious	not-distinguishable
overburden seal (585170)	DWF	turbid	not-distinguishable	distinguishable
	DWS	become clear	blurry	transitional
	2M-brine	become clear	distinguishable	transitional
	kerosene	clear	obvious	not-distinguishable
underlying sediment (590470)	DWF	turbid	not-distinguishable	distinguishable
	DWS	become clear	not-distinguishable	intermittently distinguishable
	2M-brine	become clear	distinguishable	transitional
	kerosene	N/A	N/A	N/A

Remarks.
[1)] Transitional: the accumulated interface disappears while merging into depositional interface.
[2)] Intermittently distinguishable – when the supernatant above the accumulated interface becomes clear, segregated fines gather as a thin, bright deposit on the accumulated interface that provides enough visual contrast to discern the accumulated interface, which had disappeared for a while.

participate in the sediment fabric. The final height in 2M-brine is greater than the initial 25.4 mm because all fines are involved in the final fabric.

5.6.2. Reservoir-sandy interbed (640170)

The sedimentation pattern of the reservoir-sandy interbed and reservoir-fine sand in DWS, DWF and 2M-brine are alike. However, the fines content of the reservoir-sandy interbed is high enough to generate a visible depositional interface in 2M-brine. Compared to aqueous fluids, the kerosene allows particles of all sizes to cluster and settle faster than particles in the other fluids. Sedimentation in kerosene is uniform, with a clear depositional interface, and the final height in kerosene is higher than any other cases because the rapidly-forming clusters have higher void ratios and form a loose fabric. The primary fines are quartz-type angular particles like in the reservoir-fine sand sample.

5.6.3. Reservoir-clay interbed (634470)

Whereas the reservoir-fine sand and reservoir-sandy interbed specimens have clear accumulation interfaces and demonstrate segregated sedimentation, the clay interbed samples in aqueous fluids have an accumulation interface that merges into the depositional interface and transitions toward uniform sedimentation. In DWF, the fines are better suspended and while the supernatant clears, the depositional interface is not as distinct as in DWS and 2M-brine. The ionic concentration in DWS and 2M-brine allow fines to cluster and settle on the accumulation interface. Eventually, the concentration of settling clusters increases to the point that only the deposition interface can be observed. The falling velocity of the DWF depositional interface is slower than that in kerosene, which shows rapid, fully uniform sedimentation, and 2M-brine due to ionic concentration. The final height of the reservoir-clay interbed depositional interface in DWF is the highest among the test fluids and that in 2M-brine (the highest ionic concentration) is the shortest. This final height pattern for the reservoir-clay interbed specimen is different from that of the reservoir-sandy interbed specimen, and the difference is attributed to the reservoir-clay interbed having a higher specific surface (Table 2), and higher concentrations of electrically sensitive fines such as clays in the smectite group, as inferred from the SEM images of fluffy clusters of fines even just at ambient humidity (Fig. 5e). Smectite clays adsorb water onto particle surfaces and develop a diffusive double layer, DDL. DDL thickness decreases when ionic concentration increases. These DDLs separate particles, so the thick DDL fabric in DWF forms a final interface height that is higher than that in the thinner DDL DWS and 2M-brine cases.

5.6.4. Overburden seal, diatom-rich (585170)

The depositional and accumulated interface behaviors are alike between the DWS and 2M-brine cases. Although the accumulated interface height in DWF tracks with that in DWS and 2M-brine because coarse particle sedimentation is dominated by the gravitational force, the depositional interface, which is controlled by fines, is not distinguishable in DWF, and the supernatant remains turbid. The reduced ionic concentration in DWF hinders clustering of fines, and the falling velocity in DWF is slower than that in DWS and 2M-brine. Because fines such as diatoms in the overburden seal remain suspended, they do not contribute to the final accumulated interface height in DWF, and the final accumulated height in DWF is the shortest of all the overburden tests. As seen in the other kerosene tests, particles in kerosene cluster and build high void-ratio fabrics with the tallest final interface height.

5.6.5. Underlying sediment (590470)

The segregated fines in this sample cluster and settle more rapidly in aqueous fluid when the ionic concentration increases. The supernatant in DWF is turbid even at the end of the test because fines remains in the suspension due to repulsive interparticle electrical forces. The final depositional interface heights of DWS and 2M-brine are similar to the accumulated interface height in DWF. The pattern of increasing interface height with decreasing salinity also occurred in the reservoir-clay interbed specimen, and may indicate the presence of smectite in the underlying sediment.

6. Implications

The sediment analyses in this study not only provide a basis for refining the description of geologic controls on the morphology and distribution of gas hydrate in Area B, but also elucidate how the system will respond to extracting gas hydrate-bound methane as an energy resource.

6.1. Gas hydrate morphology

Based on geologic and lithological information, gas hydrate morphology observed in Area B can be predicted based on a competition between the particle grain size (corresponding to pore size for estimating capillary pressure) and the vertical effective stress, σ_v'. In fine-grained sediment, where there is a high capillary entry pressure to overcome for gas hydrate to invade a pore, gas hydrate growth will instead occur via sediment grain displacement as gas hydrate creates and fills fractures. If the σ_v' is high enough, however, the sediment grains will be held together tightly enough for the gas hydrates to grow by invading existing pore space rather than displacing grains. Following the approach of Dai et al. (2012), a non-dimensional ratio that indicates whether displacement or invasion will dominate can be approximately defined for simple cubic packing of sediment grains as:

$$\psi \cong \frac{10\gamma_{hw}}{d_{10}\sigma_v'} = 1 \tag{3}$$

where γ_{hw}, the gas hydrate-water interfacial tension, is taken to be ~0.036 N/m (Anderson et al., 2003; Uchida et al., 1999) As ψ falls below 1, σ'_v begins to dominate. For Area B, $\psi = 0.1$ appears to represent a transition between grain displacing and pore-filling gas hydrate (Fig. 7). Fig. 7 plots the morphology based on d_{10} given by the measured grain distributions for specimens in Table 3 and with the effective vertical stress given by theoretical calculations using the specimen depth, bulk density from LWD data and an assumed water density of 1.03 g/cm^3. Though the sandy sediment layers have approximately the same d_{10} over the depth range in which they occur, the shallower sediments host fracture-filling gas hydrate owing to low vertical effective stress. This is particularly noticeable in Unit I, which generally hosts gas hydrate-filled fractures due to its fine-grained nature. At NGHP-02-19, however, Unit II's upper part, which has similar particle sizes to Unit I, is deep enough for the effective stress to be high enough for gas hydrate to form in the pore-filling morphology even in the relatively fine Unit I sediment.

6.2. Gas hydrate distribution

A critical aspect of establishing a gas hydrate reservoir's potential as an energy resource is establishing the seal conditions bounding the reservoir (Ajayi et al., 2018; Konno et al., 2019). A reservoir with poorly-sealed boundaries may be difficult to depressurize enough to induce gas hydrate dissociation. Poor seals can also allow methane to spread more broadly with depth, contributing to lower total methane hydrate saturations in the primary reservoir sediment.

For Area B, the primary reservoir is in Unit IV near the crest of the anticline. As shown in Fig. 4, however, the overlying Unit III does not provide a perfect seal that constrains gas hydrate to Unit IV alone. The SEM and smear-slide analysis indicate Unit III contains a significant concentration of diatoms, and this particular type of fines exerts an important control on host-sediment structure. The presence of diatoms allows fine-grains sediment to resist compaction (Bryant and Rack, 1990; Hamilton, 1976) and retain high porosities even at depth. As

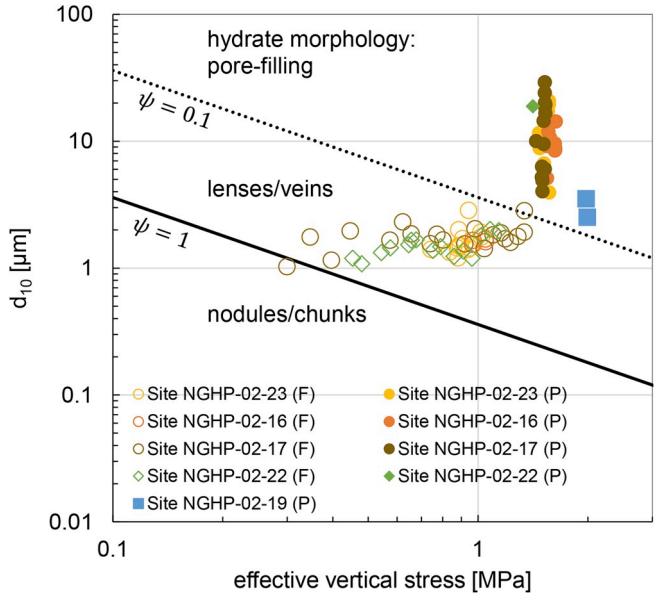

Fig. 7. Gas hydrate morphology dependence on the relationship between particle size, d_{10}, and vertical effective stress, σ'_v (Dai et al., 2012). Gas hydrate types are categorized as gas hydrate-filled fractures (F) and pore-filling (P) in this study. ψ is calculated from Eq. (2). For ψ smaller than 0.1, σ'_v dominates, holds sediment grains together, and gas hydrate grows by invading existing pore space. For higher values of ψ, gas hydrate forms more readily by displacing sediment grains. NGHP-02-19 has gas hydrate at depths of ~300mbsf, where σ'_v is high enough for pore-filling gas hydrate to form (blue squares) in sediment with grain sizes similar to those hosting grain-displacing, gas hydrate-filled fractures higher in the sediment column, where σ'_v is reduced. (For interpretation of the references to color in this figure legend, the reader is referred to the Web version of this article.)

shown in Fig. 4, porosity slightly increases with depth in Unit III. Where Unit III contacts the primary gas hydrate reservoir, the Unit III porosity is nearly 70% (Table 2), and its permeability can be expected to be high relative to a normally-compacted fine-grained sediment at that depth.

Permeability estimates for the five sediment samples tested in this study are presented in Table 6 (see Appendix for permeability equations). The permeability for the reservoir-fine sand sample, being relatively coarse and unconsolidated, is calculated based solely on elements of its grain size distribution and porosity (Table 2). As shown in the appendix, permeability decreases with decreasing grain size and porosity. The remaining samples have higher fines contents, and permeability is instead calculated using the specific surface and porosity (Table 2). As shown in the appendix, permeability decreases with increasing specific surface and decreasing porosity.

Relative to the interbed and underlying sediment, Unit III has the highest permeability in spite of the grains also having the largest specific surface area. This demonstrates the effect of the high porosity at the base of Unit III relative to that of the fine-grained interbeds in the overlying part of the unit. The estimated Unit III permeability is consistent with the modeled value, 0.05mD, used for fine-grained sediments in the NGHP-02-16 reservoir modeling of Myshakin et al. (2019). The estimate presented here is likely to be a lower bound on the actual permeability, however. The equations for calculating permeability through fine-grained sediment used here predict permeability will decrease with specific surface, and diatoms are characterized by very high specific surfaces. As shown in the SEM image, however, much of that surface area is within the diatom's structure where water will not participate in flow. If only the outer surface area of the intact diatoms were included in the permeability calculation, the estimated permeability would be driven even higher by the high porosity.

When permeability is measured directly rather than estimated from specific surface area-based equations, the presence of diatoms has been shown to dramatically increase the permeability of the fine-grained sediment in which it resides (Bryant and Rack, 1990; Spinelli et al., 2004). For the ~20% concentration of diatoms in the Unit III specimen tested here, and porosities near 70% (Table 2), Bryant and Rack (1990) report permeabilities of ~5 to 30mD. As discussed in Section 4.1, Unit III should not be viewed as an effective seal for retaining methane in the Unit IV reservoir sediment, and may even contribute water to the Unit IV reservoir if Unit IV sediment is depressurized to extract methane from gas hydrate Ajayi et al. (2018). This is particularly relevant for the primary Unit IV gas hydrate reservoir because of the potentially high driving forces for flow. As illustrated by Boswell et al. (2019), gas hydrate stability becomes less sensitive to pressure changes in deep-water environments where the in situ pore pressure is extremely high. Even though the Unit IV reservoir is near the base of gas hydrate stability (Collett et al., 2019; Waite et al., 2019-a), pressure drawdowns of more than 10 MPa are required for dissociation (Boswell et al., 2019; Myshakin et al., 2019), with ~25 MPa drawdowns recommended for optimizing the gas hydrate dissociation rates (Boswell et al., 2019; Myshakin et al., 2019).

Relative to the Unit III overburden, the Unit IV fine-grained interbeds are low permeability, raising the possibility of limiting the target depth interval for production and using the low-permeability interbeds to help isolate certain portions of the Unit IV reservoir. This type of isolation may be required to prevent the depressurization's efficiency loss due to fluid communication with the water-bearing coarse-grained sediments in the lower portion of Unit IV (Myshakin et al., 2019).

The reservoir sediment itself is predicted to have a high intrinsic permeability of 1100–1400mD in the absence of gas hydrate, in agreement with the modeling estimate of 1000mD (Myshakin et al., 2019). This is likely to be an upper bound on the intrinsic permeability because the permeability models of Amer and Awad (1974) and Chapuis (2004) are intended only for coarse-grained systems. Though permeability scales with porosity, permeability is also strongly influenced by the morphology of fines (Lambe and Whitman, 1969; Dai et al., 2019; Jang et al., 2019). As discussed in Section 5, even Area B specimens with d_{50} above 63 μm contain enough fines to be subject to flow and mechanical property control by those fines. If the reservoir fine sand specimen's permeability is calculated assuming the sediment behavior is controlled by the fine fraction rather than the coarse fraction, a lower bound on the permeability of the reservoir-fine sand specimen would be 0.05–0.14mD, calculated using the same equations

Table 6
Geotechnical parameters from index property correlations.

Sample ID	permeability [mD]	thermal conductivity [W/mK][3)]	
		parallel	series
reservoir-fine sand (633170)	1100 – 1400[1)]	1.438	0.975
reservoir-sandy interbed (640170)	.0079 – 0.025[2)]	1.483	1.017
reservoir-clay interbed (634470)	0.0036–0.0067[2)]	1.355	0.906
overburden seal (585170)	0.016 – 0.035[2)]	0.989	0.691
underlying sediment (590470)	0.0041–0.0044[2)]	1.223	0.845

[1)] Bounded by the estimates from Amer and Awad (1974) and Chapuis (2004), using their equations for unconsolidated, coarse-grained soils. See Appendix for equations.
[2)] Bounded by the estimates from Carrier (2003) and Ren and Santamarina (2018), using their equations appropriate for fine-grained sediment. See Appendix for equations.
[3)] Equation based on porosity and gas hydrate saturation (Cortes et al., 2009; Santamarina and Ruppel, 2010). Assume that gas hydrate saturation = 0.6, water saturation = 0.4. Thermal conductivity: 2 W/mK for sediment, 0.6 W/mK for water (Mitchell and Soga, 2005), 0.5 W/mK for gas hydrate (Sloan and Koh, 2007).

from Carrier (2003) and Ren and Santamarina (2018) that were used to calculate permeability for the other specimens listed in Table 6. An experimental estimate of ~100mD for a d_{50} of ~90 μm (Table 2, reservoir-fine sand) is given by the gas hydrate-free, intrinsic permeability trend through the NGHP-02 measurements by Yoneda et al. (2019-a).

6.3. Reservoir response to extracting gas hydrates

In a gas hydrate reservoir undergoing production via depressurization, two important consequences are the increasing effective stress as pore pressure is drawn down, and the pore-water freshening as gas hydrate dissociates and liberates fresh water. The formation response to an effective stress increase depends on elements of the sediment fabric, such as how the fine-grained particles contribute to sediment compressibility through their arrangement at coarse grained contacts. As observed in the electrical sensitivity and sedimentation tests, the fabric of fines depends on pore-fluid chemistry, and can therefore be expected to change as the pore water freshens during gas hydrate dissociation.

Based on Park and Santamarina's (2017) revised soil classification system, RSCS, assessment of the NGHP-02 fines properties suggests the fines in pore-filling gas hydrate-bearing sediments exist in high-enough concentrations to control mechanical responses and fluid flow within the gas hydrate reservoir. The importance of an RSCS assessment of the significance of fines in defining host sediment behavior rather than relying solely on fines content is apparent in the NGHP-02 data. Yoneda et al. (2019b) report that sediment strength is generally lower for NGHP-02 material than for gas hydrate-bearing sediments of comparable sand content, median grain size and gas-hydrate saturations collected from the Nankai Trough (Ito et al., 2015; Yoneda et al., 2019b). As noted in the RSCS (Park and Santamarina, 2017), in addition to the fines content, differences in the types of fines and their liquid limits both contribute to the impact that a given fines content will have on the host sediment behavior.

Behavior of the reservoir-sand fines appears to be dominated by small grains of quartz. By contrast, electrical sensitivity and sedimentation tests indicate the behavior of fines in the interbeds, overburden and underlying sediment is dominated by smectite, which tends to form thicker diffuse double layers (DDLs) as pore water freshens. High smectite contents (40–80%) were also observed in the Krishna-Godavari Basin during NGHP-01 (Phillips et al., 2014), so the behavior of smectite likely constitutes an issue of regional relevance rather than being specific to Area B.

Freshening during gas hydrate dissociation favors additional interparticle repulsion between the types of fines present at the Area B anticline crest. This can lead to the detachment of fines from pore walls or coarse grained contacts, particularly at the flow rates anticipated for production activities (Oyama et al., 2016). Detachment introduces fines into the fluid flowing toward the production well. Since these particles are less prone to clustering and settling when in fresh water, they are less likely to clog pore throats (Cao et al., 2019) than would be anticipated in the absence of pore-water freshening. However, because methane production requires radial flow inward toward the production well, the concentration of fines will increase along the flow path approaching the wellbore, increasing the clogging potential (Valdes and Santamarina, 2007).

In addition to providing a means of anticipating sediment behavior during pore-water freshening, the sediment characterization and RSCS sediment classification inform the choice of empirical correlations (e.g. Table 6) to estimate intrinsic geotechnical and hydraulic properties, such as the permeability (discussed above), and also thermal conductivity from the phase composition. For comparison, refer to the results of laboratory permeability experiments (Dai et al., 2019a; Jang et al., 2019; Yoneda et al., 2019a) and thermal property studies (Muraoka et al., 2019) associated with the NGHP-02 expedition.

7. Conclusions

This study provides a physical-properties-based description of the gas hydrate occurrences associated with a buried anticline-syncline system that dominates Area B in the Krishna-Godavari Basin, offshore India. Five sites were cored in Area B during NGHP-02, which was conducted to investigate geologic controls on the distribution of gas hydrate in the region. Logging while drilling (LWD), seismic and lithologic data suggest the relatively coarse-grained lithologic Unit IV likely provides a permeable pathway for methane to migrate up an anticline flank to collect primarily near the anticline crest (Collett et al., 2019; Saito et al., 2019). Unit II may also be acting as a methane conduit (Saito et al., 2019), but this inference is less certain. Unit II thins out near the crest of the anticline, but Unit IV becomes horizontal and appears to span the anticline crest just above the base of gas hydrate stability to form a highly gas-hydrate saturated reservoir between ~270 and 290mbsf. This fine-sand reservoir, thinly interbedded with fine-grained, low gas-hydrate saturation interbeds, is the primary gas hydrate reservoir in Area B.

Resistivity-based estimates of the gas hydrate saturations (Collett et al., 2019) indicate the Unit IV reservoir is only partially filled, in part because of an inefficient seal that allows methane to migrate into the overlying layer, through Unit III and into Unit I at the anticline crest, forming fracture-filled gas hydrates to within ~175mbsf. Down the flank of the anticline, Unit IV plunges below the base of gas hydrate stability, and the primary gas hydrate occurrences become generally limited to gas hydrate-filled fractures in Units I and III. Methane is likely migrating up the anticline flank through Unit IV, and possibly Unit II, and can bleed off along the way, promoting the growth of gas hydrate-filled fractures in Units I and III. Continuing off the anticline and into the syncline, a very limited gas hydrate occurrence (< 10 m-thick) formed at the top of Unit II. At all sites, it appears that the available reservoir sediment is only partly saturated with gas hydrate.

When gas hydrate forms in fine-grained sediment, it can be easier to displace sediment grains and produce a gas hydrate-filled fracture than to form gas hydrate in existing pore space. As the vertical effective stress increases at greater subsurface depths, however, sediment grains are held together more tightly, and gas hydrate growth must advance by invading existing pore space. This transition can be observed in Unit I and II, which have gas hydrate in sediments with similar grain size. Unit I sediments are shallow enough for grain-displacing gas hydrate form, but at Site NGHO-02-19, the upper part of Unit II is deep enough that the increased in situ effective stress from the overburden holds the sediment together while gas hydrate forms in a pore-filling morphology in spite of the small grain size.

Additional sediment testing of an overburden sample from the anticline crest indicates gas hydrate can form in the fine-grained Unit III above the primary coarse-grained Unit IV reservoir because the abundance of diatoms in Unit III is able to maintain high sediment porosities. These diatoms are also responsible for the unusual LWD porosity log results, which increase with the depth in Unit III on the anticline crest (porosity at the base of Unit III at the contact with reservoir Unit IV is 70%). Accordingly, they affect sediment physical properties and the gas hydrate occurrence/morphology in seal layers. At the crest of the anticline, methane appears to be able to migrate from the Unit IV reservoir and into the high-porosity, fine-grained overburden, Unit III.

A series of vertical faults and fractures also penetrate the lower units at the anticline crest, providing potential pathways for methane to move out of the Unit IV reservoir and into Unit I near 150mbsf where the faults and fractures appear to terminate. This is also approximate top of the observed gas hydrate occurrences, and it is inferred that above this depth, the fine-grained Unit I permeability drops enough to limit additional methane loss from the system. Even with methane potentially migrating to the anticline crest through Unit IV, the coarse-grained Unit IV saturation is incomplete. The distribution of coarse-grained reservoir sediment on the anticline crest is too broad, and the

overlying sediment is too permeable, for the existing methane supply to fully saturate Unit IV. Neither the top nor bottom of the Unit IV gas hydrate reservoir is well sealed, because the lower portion of Unit IV is water-bearing, relatively coarse-grained sediment that underlies the primary gas-hydrate reservoir on the anticline crest.

A soil classification study of recovered coarse-grained Area B sediment, including the fine sands in the primary gas hydrate reservoir at the anticline crest, reveals that fine-grained sediments in the coarse-grained reservoirs, as well as in the seal layers, will control many of the physical properties of the sediments, such as hydraulic conductivity, compressibility and shear strength. The fine-grain control is evident when considering gas hydrate morphology and distribution in Area B. Recognizing the control that fines exert also provides a basis for constraining the response of the primary gas hydrate reservoir to a depressurization-style methane production scenario.

For further study of each layer in the gas hydrate reservoir structure, five core samples, each characterized as either a reservoir sand, interbed or seal sediment, underwent geotechnical testing including electrical sensitivity and additional sedimentation testing. In combination with smear slide and SEM analysis, the presence of electrically sensitive fines such as smectite were established in a clay interbed and in the sediment underlying the Unit IV reservoir.

Consequences of pore-water freshening during gas extraction include the detachment of fines from larger grains, even in the reservoir sands. Detached fines are resuspended and cause an increase in the concentration of fines in the pore fluid that is swept toward the production well when extracting methane from gas hydrate as an energy resource. Increasing fines concentration as the radial flow reaches the production well could lead to clogging and thus to reduced production.

Acknowledgements

The author(s) wish to thank those that contributed to the success of the National Gas Hydrate Program Expedition 02 (NGHP-02). NGHP-02 was planned and managed by the Oil and Natural Gas Corporation Limited India (ONGC) on the behalf of the India National Gas Hydrate Program through Directorate General of Hydrocarbons (DGH) under the Ministry of Petroleum and Natural Gas (India). The drilling platform, *D/V Chikyu*, was operated by the Japanese Drilling Company (JDC) and the shipboard science program was managed by the Japan Agency for Marine-Earth Science and Technology (JAMSTEC). LWD, wireline logging, and formation testing services were provided by Schlumberger. Pressure coring tools were provided by JAMSTEC, and shipboard pressure core operations and analysis were provided by Geotek Coring. Additional operational and scientific support was provided by the U.S. Geological Survey, the U.S. Department of Energy, the National Institute of Advanced Industrial Science and Technology, and the Japan Oil, Gas and Metals National Corporation (JOGMEC). The financial support for the NGHP-02, from the Oil Industry Development Board, Oil and Natural Gas Corporation Limited is gratefully acknowledged. We also acknowledge the support extended by all the participating organizations of the NGHP: MoP&NG, DGH, ONGC, GAIL, OIL, NIO, and NIOT. This work was also supported by the Energy, and the Coastal and Marine Science Programs of the U.S. Geological Survey, with additional funding from US-DOE Interagency Agreement: DE-FE00-26166. This report was prepared as an account of work sponsored by an agency of the United States Government. The authors wish to thank B. Buczkowski and J. Chaytor (USGS) for performing XRD analyses for this study, and C. Ruppel (USGS) for constructive comments on the manuscript. Any use of trade, firm or product names is for descriptive purposes only and does not imply endorsement by the U.S. Government. Data are available online from the U. S. Geological Survey's Science Base Catalog (Jang et al., 2018c; Waite et al., 2018c).

Appendix

To estimate permeability from sediment index properties, two sets of equations are used. The first set is appropriate for coarse-grained sediments, and is based on various aspects of the grain size and porosity (expressed in terms of the void ratio). The second set of permeability equations includes the effect of surface area has a hindrance to flow, reducing permeability, and can be used for fine-grained sediments. All permeability equations presented below have had their prefactors modified to yield permeability in millidarcy [mD] (1mD is $9.869 \times 10^{-16}\,m^2$).

The conversion from unitless porosity, n (Table 2), to the void ratio, e, is:

$$e = \frac{n}{1-n} \tag{A1}$$

Case 1: Coarse-grained sediment

Permeability in coarse-grained sediments is calculated in this work using two approaches, both using the convention that the d_{10} and/or d_{60} grain sizes are in [mm] (Table 2).

The first empirical approach is from Amer and Awad (1974). The ratio d_{60}/d_{10} is defined as the coefficient of uniformity, C_u:

$$k\,[mD] = (35{\cdot}1.16\text{x}10^{6}){\cdot}\left(\frac{e^3}{1+e}\right){\cdot}\left(\frac{d_{60}}{d_{10}}\right)^{0.6}{\cdot}(d_{10})^{2.32} = (4.06\text{x}10^{7}){\cdot}\left(\frac{e^3}{1+e}\right){\cdot}(C_u)^{0.6}{\cdot}(d_{10})^{2.32} \tag{A2}$$

The second permeability formulation for coarse grained sediment is from Chapuis (2004):

$$k\,[mD] = 2.4622{\cdot}\left(d_{10}^2{\cdot}\left(\frac{e^3}{1+e}\right)\right)^{0.7825} \tag{A3}$$

Case 2: Fine-grained sediment

Determination of permeability in fine grained sediment relies on the grain specific surface, S_s, rather than grain size. Specific surface is given in Table 2 with units of [m^2/g], but in the formulation from Carrier (2003), specific surface, $S_{s,Carrier}$, is given in units of [1/cm]. The conversion uses the sediment grain density, ρ_{grain} [kg/m^3] (Table 2):

$$k\,[mD] = (1.99\text{x}10^{4}{\cdot}1.16\text{x}10^{6}){\cdot}\left(\frac{e^3}{1+e}\right){\cdot}\left(\frac{1}{S_{s,Carrier}^2}\right) \tag{A4}$$

$$S_{s,\,Carrier}\left[\frac{1}{cm}\right] = S_s\left[\frac{m^2}{g}\right]\cdot\rho_{grain}\left[\frac{kg}{m^3}\right]\cdot 10 \tag{A5}$$

The second fine-grained permeability equation used in this study is from Ren and Santamarina (2018) and uses S_s [m^2/g], as it is presented in Table 2:

$$k\,[mD] = (11.6)\cdot\left(\frac{1}{S_s^2}\right)\cdot e^{\beta}, \tag{A6}$$

$$\beta = 4 \tag{A7}$$

The exponent, β, which controls the sensitivity of permeability to void ratio, increases with increasing S_s (Ren and Santamarina, 2018). Above $S_s = 1\ m^2/g$, β is nearly constant and is simply taken here as 4 for all specimens. Choosing $\beta = 2.35$ very nearly reproduces the Carrier (2003) results from (A4) (Ren and Santamarina, 2018).

References

Adolph, B., Stoller, C., Archer, M., Codazzi, D., el-Halawani, T., Perciot, P., Weller, G., Evans, M., Grant, J., Griffiths, R., Hartman, D., Sirkin, G., Ichikawa, M., Scott, G., Tribe, I., White, D., 2005. No more waiting: formation evolution while drilling. Oilfield Rev. 17, 4–21.

Ajayi, T., Anderson, B.J., Seol, Y., Boswell, R., Myshakin, E.M., 2018. Key aspects of numerical analysis of gas hydrate reservoir performance: Alaska North Slope Prudhoe Bay Unit "L-Pad" hydrate accumulation". J. Nat. Gas Sci. Eng. 51, 37–43.

Amer, A.M., Awad, A.A., 1974. Permeability of cohesionless soils. Journal of Geotechnical Engineering Division, American Society of Civil Engineers 100 (GT12), 1309–1326.

Anderson, R., Llamedo, M., Tohidi, B., Burgass, R.W., 2003. Experimental measurement of methane and carbon dioxide clathrate hydrate equilibria in mesoporous silica. J. Phys. Chem. B 107 (15), 3507–3514.

ASTM, 2005. Standard Test Methods for Liquid Limit, Plastic Limit, and Plasticity Index of Soils. ASTM D4318, West Conshohocken, PA.

Bonner, S., Fredette, M., Lovell, J., Montaron, B., Rosthal, R., Tabanou, J., Wu, P., Clark, B., Mills, R., Williams, R., 1996. Resistivity while drilling-images from the string. Oilfield Rev. 8, 4–19.

Boswell, R., Collett, T.S., Frye, M., Shedd, W., McConnell, D.R., Shelander, D., 2012. Subsurface gas hydrates in the northern Gulf of Mexico. Mar. Petrol. Geol. 34 (1), 4–30.

Boswell, R., Myshakin, E., Moridis, G., Konno, Y., Collett, T.S., Reagan, M., Ajayi, T., Seol, Y., 2019. India National Gas Hydrate Program Expedition 02 summary of scientific results: numerical simulation of reservoir response to depressurization. J. Mar. Petrol. Geol. 108, 154–166.

British Standard Insitute BSI, 1990. Methods of Test for Soils for Civil Engineering Purpose, vol. 1377 BS, London.

Bryant, W.R., Rack, F.R., 1990. Consolidatin and characteristics of weddell sea sediments: results of ODP leg 113. In: In: Barker, P.F., Kennett, J.P. (Eds.), Proceedings of the Ocean Drilling Program, Scientific Results, vol. 113. Ocean Drilling Program, College Station, TX, pp. 211–223.

Cao, S.C., Jang, J., Jung, J., Waite, W.F., Collett, T.S., Kumar, P., 2019. 2D micromodel study of clogging behavior of fine-grained particles associated with gas hydrate production in NGHP-02 gas hydrate reservoir sediments. J. Mar. Petrol. Geol. 108, 714–730.

Carrier, W.D., 2003. Goodbye, hazen; hello, kozeny-carman. J. Geotech. Geoenviron. Eng. 129 (11), 1054–1056.

Chapuis, R.P., 2004. Predicting the saturated hydraulic conductivity of sand and gravel using effective diameter and void ratio. Can. Geotech. J. 41 (5), 787–795.

Cho, G.C., Dodds, J., Santamarina, J.C., 2006. Particle shape effects on packing density, stiffness, and strength: natural and crushed sands. J. Geotech. Geoenviron. Eng. 132 (5), 591–602.

Collett, T., Reidel, M., Cochran, J., Boswell, R., Presley, J., Kumar, P., Sathe, A., Sethi, A., Lall, M., Sibal, V., the NGHP Expedition 01 Scientists, 2008. Indian National Gas Hydrate Program Expedition 01 Initial Reports: Expedition 01 of the Indian National Gas Hydrate Program from Mumbai, India to Chennai, India; Sites NGHP-01-01 through NGHP-01-21, April 2006 - August 2006. Directorate General of Hydrocarbons, Ministry of Petroleum and Natural Gas (India), Noida, India.

Collett, T.S., Boswell, R., Cochran, J.R., Kumar, P., Lall, M., Mazumdar, A., Ramana, M.V., Ramprasad, T., Riedel, M., Sain, K., Sathe, A.V., Vishwanath, K., NGHP Expedition 01 Science Party, 2014. Geologic implications of gas hydrates in the offshore of India: results of the national gas hydrate program expedition 01. Mar. Petrol. Geol. 58, 3–28.

Collett, T.S., Johnson, A.H., Knapp, C.C., Boswell, R., 2009. Natural gas hydrates: a review. In: Collett, T.S., Johnson, A.H., Knapp, C.C., Boswell, R. (Eds.), Natural Gas Hydrates - Energy Resource Potential and Associated Geologic Hazards, pp. 146–219 AAPG Memoir 89.

Collett, T.S., Boswell, R., Waite, W.F., Kumar, P., Roy, S.K., Chopra, K., Singh, S.K., Yamada, Y., Tenma, N., Pohlman, J., Zyrianova, M., NGHP Expedition 02 Scientific Party, 2019. India National Gas Hydrate Program Expedition 02 summary of scientific results: gas hydrate systems along the eastern continental margin of India. J. Mar. Petrol. Geol. 108, 39–142.

Collett, T.S., Kvenvolden, K., 1988. Natural gas hydrate. In: Magoon, L.B. (Ed.), Petroleum Systems of the United States. U. S. Geological Survey Bulletin, pp. 46–47 1870.

Cook, A.E., Anderson, B.I., Malinverno, A., Mrozewski, S., Goldberg, D.S., 2010. Electrical anisotropy due to gas hydrate-filled fractures. Geophysics 75 (6), F173–F185.

Cortes, D.D., Martin, A.I., Yun, T.S., Francisca, F.M., Santamarina, J.C., Ruppel, C., 2009. Thermal conductivity of hydrate-bearing sediments. J. Geophys. Res. 114 (B11103).

Dai, S., Kim, J., Xu, Y., Waite, W., Jang, J., Yoneda, J., Collett, T.S., Kumar, P., 2019. Permeability anisotropy and relative permeability in sediments from expedition NGHP-02 offshore India. J. Mar. Petrol. Geol. 108, 705–713.

Dai, S., Santamarina, J.C., Waite, W.F., Kneafsey, T.J., 2012. Hydrate morphology: physical properties of sands with patchy hydrate saturation. J. Geophys. Res. 117, B11205.

Dixit, G., Ram, H., Kumar, P., et al., 2019. Origin of gas in gas hydrates as interpreted from geochemistry data obtained during the National Gas Hydrate Program Expedition 02, Krishna Godavari Basin, offshore India. J. Mar. Petrol. Geol. 108, 386–396.

Expedition 331 Scientists, 2011. Methods. In: In: Takai, K., Mottl, M.J., Nielsen, S.H., the Expedition 331 Scientists (Eds.), Proceedings of the Integrated Ocean Drilling Program, vol. 331 (Tokyo).

Folk, R.L., 1954. The distinction between grain size and mineral composition in sedimentary-rock nomenclature. J. Geol. 62 (4), 344–359.

Hamilton, E.L., 1976. Variations of density and porosity with depth in deep-sea sediments. J. Sediment. Petrol. 46 (2), 280–300.

Henry, P., Thomas, M., Ben Clennell, M., 1999. Formation of natural gas hydrates in marine sediments 2. Thermodynamic calculations of stability conditions in porous sediments. Journal of Geophysical Research-Solid Earth 104 (B10), 23005–23022.

Hesse, R., Harrison, W.E., 1981. Gas hydrates (clathrates) causing pore-water freshening and oxygen isotope fractionation in deep-water sedimentary sections of terrigenous continental margins. Earth Planet Sci. Lett. 55 (3), 453–462.

Holland, M., Schultheiss, P., Roberts, J., 2019. Gas hydrate saturation and morphology from analysis of pressure cores acquired in the Bay of Bengal during expedition NGHP-02, offshore India. J. Mar. Petrol. Geol. 108, 407–423.

Hsiung, K.H., Saito, S., Kanamatsu, T., Sanada, Y., Yamada, Y., NGHP Expedition 02 JAMSTEC Science Team, 2019. Regional stratigraphic framework and gas hydrate occurrence Offshore Eastern India: Core-log-seismic integration of national gas hydrate program Expedition 02 (NGHP-02) Area-B Drill Sites. J. Mar. Petrol. Geol. 108, 206–215.

Ito, T., Komatsu, Y., Fujii, T., Suzuki, K., Egawa, K., Nakatsuka, Y., Konno, Y., Yoneda, J., Jin, Y., Kida, M., Nagao, J., Minagawa, H., 2015. Lithological features of hydrate-bearing sediments and their relationship with gas hydrate saturation in the eastern Nankai Trough, Japan. Mar. Petrol. Geol. 66, 368–378.

Jain, A.K., Juanes, R., 2009. Preferential Mode of gas invasion in sediments: grain-scale mechanistic model of coupled multiphase fluid flow and sediment mechanics. Journal of Geophysical Research-Solid Earth 114, B08101.

Jang, J., Cao, S.C., Stern, L.A., Jung, J., Waite, F.W., 2018a. Impact of pore-fluid chemistry on fine-grained sediment fabric and compressibility. J. Geophys. Res.: Solid Earth 123, 5495–5514.

Jang, J., Dai, S., Yoneda, J., Waite, W.F., Stern, L., Boze, L., Collett, T.S., Kumar, P., 2019. Pressure core analysis of geomechanical and fluid flow properties of seals associated with gas hydrate-bearing reservoirs in the Krishna-Godavari Basin, offshore India. J. Mar. Petrol. Geol. 108, 537–550.

Jang, J., Santamarina, J.C., 2016. Fines classification based on sensitivity to pore-fluid chemistry. J. Geotech. Geoenviron. Eng. 142 (4), 06015018.

Jang, J., Santamarina, J.C., 2017. Closure to "fines classification based on sensitivity to pore-fluid chemistry" by junbong Jang and J. Carlos Santamarina. J. Geotech. Geoenviron. Eng. 143 (7), 07017013.

Jang, J., Waite, F.W., Stern, L.A., Collett, T.S., Kumar, P., 2018c. Dependence of sedimentation behavior on pore-fluid chemistry for sediment collected from area B, Krishna-Godavari Basin during India's national gas hydrate program, NGHP-02. U. S. Geological Survey data release. https://doi.org/10.5066/P9FXJ1VX.

Joshi, A.K., Sain, K., Pandey, L., Schlumberger-Representatives, 2019. Gas hydrate saturation and reservoir characterization at sites NGHP-02-17 and NGHP-02-19, Krishna Godavari Basin, eastern margin of India. J. Mar. Petrol. Geol. 108, 595–608.

Konno, Y., Kato, A., Yoneda, J., Oshima, M., Kida, M., Jin, Y., Nagao, J., Tenma, N., 2019. Numerical analysis of gas production potential from a gas-hydrate reservoir at Site NGHP-02-16, the Krishna–Godavari Basin, offshore India–Feasibility of depressurization method for ultra-deepwater environment. J. Mar. Petrol. Geol. 108, 731–740.

Kraemer, L.M., Owen, R.M., Dickens, G.R., 2000. Lithology of the upper gas hydrate zone, Blake Oouter Ridge: a link between diatoms, porosity, and gas hydrate. In: In: Paull, C.K., Matsumoto, R., Wallace, P.J., Dillon, W.P. (Eds.), Proceedings of the Ocean

Drilling Program, Scientific Results, vol. 164. pp. 229–236.
Kumar, P., Collett, T.S., et al., 2019. India National Gas Hydrate Program Expedition-02: operational and technical summary. J. Mar. Petrol. Geol. 108, 3–38.
Kvenvolden, K., 1993. Gas hydrates - geological perspective and global change. Rev. Geophys. 31 (2), 173–187.
Lambe, T.W., Whitman, R.V., 1969. Soil Mechanics. John Wiley & Sons, New York.
Lee, M.W., Collett, T., 2011. In-situ gas hydrate hydrate saturation estimated from various well logs at mount elbert gas hydarte stratigraphic test well, alask north slope. Mar. Petrol. Geol. 28, 439–449.
Lee, M.W., Collett, T.S., 2009. Gas hydrate saturations estimated from fractured reservoir at Site NGHP-01-10, Krishna-Godavari Basin, India. Journal of Geophysical Research-Solid Earth 114, B07102.
Lin, J.S., Uchida, S., Myshakin, E., Seol, Y., Rutqvist, J., Boswell, R., 2019. Assessing the geomechanical stability of interbedded hydrate-bearing sediments under gas production by depressurization at site NGHP-02-16. J. Mar. Petrol. Geol 108, 648–659.
Magoon, L.B., 1988. The petroleum system - a classification scheme for research, exploration, and resource assessment. In: Magoon, L.B. (Ed.), Petroleum Systems of the United States. U. S. Geological Survey Bulletin, pp. 2–15 1870.
Max, M.D., Johnson, A.H., 2014. Hydrate petroleum system approach to natural gas hydrate exploration. Petrol. Geosci. 20 (2), 187–199.
McBride, M.B., Baveye, P., 2002. Diffuse double-layer models, long-range forces, and ordering in clay colloids. Soil Sci. Soc. Am. J. 66 (4), 1207–1217.
Miklasz, K.A., Denny, M.W., 2010. Diatom sinking speeds: improved predictions and insight from a modified Stokes' law. Limnol. Oceanogr. 55 (6), 2513–2525.
Mitchell, J.K., Soga, K., 2005. Fundamentals of Soil Behavior. John Wiley & Sons, Inc.
Muraoka, M., Ohtake, M., Susuki, N., Morita, H., Ohshima, M., Yamamoto, Y., 2019. Thermal properties of highly saturated methane hydrate-bearing sediments recovered from the Krishna-Godavari and Mahanadi Basins. J. Mar. Petrol. Geol 108, 321–331.
Musgrave, R.J., Bangs, N.L., Larrasoana, J.C., Gracia, E., Hollamby, J.A., Vega, M.E., 2006. Rise of the base of the gas hydrate zone since the last glacial recorded by rock magnetism. Geology 34 (2), 117–120.
Myshakin, E.M., Seol, Y., Lin, J.S., Uchida, S., Collett, T.S., Boswell, R., 2019. Numerical simulations of depressurization-induced gas production from an interbedded turbidite gas hydrate-bearing sedimentary section in the offshore India: Site NGHP-02-16 (Area-B). J. Mar. Petrol. Geol. 108, 619–638.
Nanda, J., Shukla, K.M., Lall, M.V., Yadav, U.S., Kumar, P., et al., 2019. Lithofacies characterization of gas hydrate prospects discovered during the National Gas Hydrate Program Expedition 02. J. Mar. Petrol. Geol 108, 226–238.
Oshima, M., Suzuki, K., Yoneda, J., Kato, A., Kida, M., Konno, Y., Muraoka, M., Jin, Y., Nagao, J., Tenma, N., 2019. Lithological properties of natural gas hydrate–bearing sediments in pressure-cores recovered from the Krishna–Godavari Basin. J. Mar. Petrol. Geol. 108, 439–470.
Oyama, H., Abe, S., Yoshida, T., Sato, T., Nagao, J., Tenma, N., Narita, H., 2016. Experimental study of mud erosion at the interface of an artificial sand-mud alternate layer. J. Nat. Gas Sci. Eng. 34, 1106–1114.
Palomino, A.M., Santamarina, J.C., 2005. Fabric map for kaolinite: effects of pH and ionic concentration on behavior. Clay Clay Miner. 53 (3), 209–222.
Park, J., Santamarina, J.C., 2017. Revised soil classification system for coarse-fine mixtures. J. Geotech. Geoenviron. Eng. 143 (8), 04017039.
Perry, W.J., 1988. Structure. In: Magoon, L.B. (Ed.), Petroleum Systems of the United States. U. S. Geological Survey Bulletin, pp. 36–38 1870.
Phillips, S.C., Johnson, J.E., Underwood, M.B., Guo, J.H., Giosan, L., Rose, K., 2014. Long-timescale variation in bulk and clay mineral composition of Indian continental margin sediments in the Bay of Bengal, Arabian Sea, and Andaman Sea. Mar. Petrol. Geol. 58, 117–138.
Pierre, A.C., Ma, K., 1999. DLVO theory and clay aggregate architectures formed with AlCl3. J. Eur. Ceram. Soc. 19 (8), 1615–1622.
Poppe, L.J., Paskevich, V.F., Hathaway, J.C., Blackwood, D.S., 2001. A Laboratory Manual for X-ray Powder Diffraction. U.S. Geological Survey Open-file Report 01-041. U.S. Geological Survey.
Radhakrishna, M., Twinkle, D., Nayak, S., Bastia, R., Rao, G.S., 2012. Crustal structure and rift architecture across the Krishna-Godavari basin in the central Eastern Continental Margin of India based on analysis of gravity and seismic data. Mar. Petrol. Geol. 37 (1), 129–146.
Rao, G.N., 2001. Sedimentation, stratigraphy, and petroleum potential of Krishna-Godavari basin, East Coast of India. AAPG (Am. Assoc. Pet. Geol.) Bull. 85 (9), 1623–1643.
Ren, X.W., Santamarina, J.C., 2018. The hydraulic conductivity of sediments: a pore size perspective. Eng. Geol. 233, 48–54.
Ryu, B.J., Collett, T.S., Riedel, M., Kim, G.Y., Chun, J.H., Bahk, J.J., Lee, J.Y., Kim, J.H., Yoo, D.G., 2013. Scientific results of the second gas hydrate drilling expedition in the Ulleung Basin (UBGH2). Mar. Petrol. Geol. 47, 1–20.
Saito, S., Hsiung, K.H., Sanada, Y., Moe, K., Hamada, Y., Nakamura, Y., Wu, H.Y., Shinmoto, Y., Yamada, Y., NGHP Expedition 02 JAMSTEC Science Team, 2019. Gas hydrate occurrence and distribution controlled by regional geological structure off Eastern India: Estimate form logging-while-drilling in Area B, National Gas Hydrate Program Expedition 02 (NGHP-02). J. Mar. Petrol. Geol. 108, 216–225.
Santamarina, J.C., Klein, K.A., Wang, Y.H., Prencke, E., 2002. Specific surface: determination and relevance. Can. Geotech. J. 39, 233–241.
Santamarina, J.C., Ruppel, C., 2010. The impact of hydrate saturation on the mechanical, electrical, and thermal properties of hydrate-bearing sand, silts, and clay. In: Riedel, M., Willoughby, E.C., Chopra, S. (Eds.), Geophysical Characterization of Gas Hydrates. Society of Exploration Geophysicists, Tulsa, OK, pp. 373–384.
Schlumberger, 2006. ECS Elemental Capture Spectroscopy Sonde. available at: http://www.slb.com/~/media/Files/evaluation/brochures/wireline_open_hole/petrophysics/porosity/ecs_brochure.pdf.
Shankar, U., 2016. Gas hydrate saturation from seismic data constrained by log data in the Krishna-Godavari Basin. J. Petrol. Explor. Prod. Technol. 6 (1), 13–23.
Shukla, K.M., Kumar, P., Yadav, U.S., NGHP-02 Science team, 2019a. Gas hydrate reservoir identification, delineation, and characterization in the Krishna-Godavari basin using subsurface geologic and geophysical data from the national gas hydrate program 02 expedition, offshore India. J. Mar. Petrol. Geol. 108, 185–205.
Shukla, K.M., Yadav, U.S., Kumar, P., Collett, T.S., Boswell, R., Frye, M., Riedel, M., Kaur, I., Vishwanath, K., 2019b. National gas hydrate program Expedition 02: Identification of gas hydrate prospects in the Krishna-Godavari Basin, Offshore India. J. Mar. Petrol. Geol. 108, 185–205.
Sloan, E.D., Koh, C.A., 2007. Clathrate Hydrates of Natural Gases. CRC Press, Taylor & Francis Group, LLC, New York.
Sogami, I., Ise, N., 1984. On the electrostatic interaction in macroionic solutions. J. Chem. Phys. 81 (12), 6320–6332.
Spinelli, G.A., Giambalvo, E.R., Fisher, A., 2004. Sediment permeability, distribution, and influence on fluxes in oceanic basement. In: Davis, E.E., Elderfield, H. (Eds.), Hydrogeology of the Oceanic Lithosphere. Cambridge University Press, Cambridge, UK, pp. 151–188.
Spinelli, G.A., Mozley, P.S., Tobin, H.J., Underwood, M.B., Hoffman, N.W., Bellew, G.M., 2007. Diagenesis, sediment strength, and pore collapse in sediment approaching the Nankai Trough subduction zone. Geol. Soc. Am. Bull. 119 (3–4), 377–390.
Sundal, A., Nystuen, J.P., Rorvik, K.L., Dypvik, H., Aagaard, P., 2016. The lower jurassic johansen formation, northern north sea - depositional model and reservoir characterization for CO2 storage. Mar. Petrol. Geol. 77, 1376–1401.
Torres, M.E., Trehu, A.M., Cespedes, N., Kastner, M., Wortmann, U.G., Kim, J.H., Long, P., Malinverno, A., Pohlman, J.W., Riedel, M., Collett, T., 2008. Methane hydrate formation in turbidite sediments of northern Cascadia, IODP Expedition 311. Earth Planet Sci. Lett. 271 (1–4), 170–180.
Uchida, S., Lin, J.-S., Myshakin, E.M., Seol, Y., Boswell, R., 2019. Numerical simulations of sand migration during gas production in hydrate bearing sands interbedded with thin mud layers at site NGHP-02-16. J. Mar. Petrol. Geol. 108, 639–647.
Uchida, T., Ebinuma, T., Ishizaki, T., 1999. Dissociation condition measurements of methane hydrate in confined small pores of porous glass. J. Phys. Chem. B 103 (18), 3659–3662.
Uchida, T., Waseda, A., Namikawa, T., 2009. Methane accumulation and high concentration of gas hydrate in marine and terrestrial sandy sediments. In: In: Collett, T., Johnson, A., Knapp, C., Boswell, R. (Eds.), Natural Gas Hydrates - Energy Resource Potential and Associated Geologic Hazard, vol. 89. AAPG Memoir, pp. 401–413.
Valdes, J.R., Santamarina, J.C., 2007. Particle transport in a nonuniform flow field: retardation and clogging. Appl. Phys. Lett. 90 (24), 244101.
Waite, W.F., Ruppel, C., Collett, T.S., Schultheiss, P., Holland, M., Shukla, K.M., Kumar, P., 2019a. Multi-measurement approach for establishing the base of gas hydrate occurrence in the Krishna-Godavari Basin for sites cored during expedition NGHP-02 in the offshore of India. J. Mar. Petrol. Geol. 108, 296–320.
Waite, W.F., Jang, J., Collett, T.S., Kumar, P., 2019b. Downhole physical property-based description of a gas hydrate petroleum system in NGHP-02 Area C: A channel, levee, fan complex in the Krishna-Godavari Basin offshore eastern India. J. Mar. Petrol. Geol. 108, 272–295.
Waite, W.F., Jang, J., Collett, T.S., Kumar, P., 2018. Grain-size Data from India's National Gas Hydrate Program NGHP-02 Expedition in the Krishna-godavari Basin Offshore Eastern India, 2015. U. S. Geological Survey data release. https://doi.org/10.5066/P97RL4X4.
Wiemer, G., Dziadek, R., Kopf, A., 2017. The enigmatic consolidation of diatomaceous sediment. Mar. Geol. 385, 173–184.
Winters, W.J., Wilcox-Cline, R.W., Long, P., Dewri, S.K., Kumar, P., Stern, L., Kerr, L., 2014. Comparison of the physical and geotechnical properties of gas-hydrate-bearing sediments from offshore India and other gas-hydrate-reservoir systems. Mar. Petrol. Geol. 58, 139–167.
Xu, W.Y., Ruppel, C., 1999. Predicting the occurrence, distribution, and evolution of methane gas hydrate in porous marine sediments. J. Geophys. Res. Solid Earth 104 (B3), 5081–5095.
Yoneda, J., Oshima, M., Kida, M., Kato, A., Konno, Y., Jin, Y., Jang, J., Waite, W.F., Kumar, P., Tenma, N., 2019a. Permeability variation and anisotropy of gas hydrate-bearing pressure-core sediments recovered from the Krishna -Godavari Basin, offshore India. J. Mar. Petrol. Geol. 108, 524–536.
Yoneda, J., Oshima, M., Kida, M., Kato, A., Konno, Y., Jin, Y., Jang, J., Waite, W., Kumar, P., Tenma, N., 2019b. Pressure core based onshore laboratory analysis on mechanical properties of hydrate-bearing sediments recovered during India's National Gas Hydrate Program Expedition (NGHP) 02. J. Mar. Petrol. Geol. 108, 482–501.
Yun, T.S., Francisca, F.M., Santamarina, J.C., Ruppel, C., 2005. Compressional and shear wave velocities in uncemented sediment containing gas hydrate. Geophys. Res. Lett. 32 (10).